

## The formation of turbidity maximum zones by minor axis tidal straining in regions of freshwater influence

Flores, Raúl P.; Rijnsburger, Sabine; Horner-Devine, Alexander R.; Kumar, Nirimesh; Souza, Alejandro J.; Pietrzak, Julie D.

**DOI**

[10.1175/JPO-D-18-0264.1](https://doi.org/10.1175/JPO-D-18-0264.1)

**Publication date**

2020

**Document Version**

Final published version

**Published in**

Journal of Physical Oceanography

**Citation (APA)**

Flores, R. P., Rijnsburger, S., Horner-Devine, A. R., Kumar, N., Souza, A. J., & Pietrzak, J. D. (2020). The formation of turbidity maximum zones by minor axis tidal straining in regions of freshwater influence. *Journal of Physical Oceanography*, 50(5), 1265-1287. <https://doi.org/10.1175/JPO-D-18-0264.1>

**Important note**

To cite this publication, please use the final published version (if applicable).  
Please check the document version above.

**Copyright**

Other than for strictly personal use, it is not permitted to download, forward or distribute the text or part of it, without the consent of the author(s) and/or copyright holder(s), unless the work is under an open content license such as Creative Commons.

**Takedown policy**

Please contact us and provide details if you believe this document breaches copyrights.  
We will remove access to the work immediately and investigate your claim.

# The Formation of Turbidity Maximum Zones by Minor Axis Tidal Straining in Regions of Freshwater Influence

RAÚL P. FLORES

*Department of Civil and Environmental Engineering, University of Washington, Seattle, Washington, and  
Departamento de Obras Civiles, Universidad Técnica Federico Santa María, Valparaíso, Chile*

SABINE RIJNSBURGER

*Department of Hydraulic Engineering, Delft Institute of Technology, Delft, Netherlands*

ALEXANDER R. HORNER-DEVINE AND NIRNIMESH KUMAR

*Department of Civil and Environmental Engineering, University of Washington, Seattle*

ALEJANDRO J. SOUZA

*CINVESTAV, Mérida, Mexico*

JULIE D. PIETRZAK

*Department of Hydraulic Engineering, Delft Institute of Technology, Delft, Netherlands*


(Manuscript received 3 January 2019, in final form 27 December 2019)

## ABSTRACT

This study investigates the influence of tidal straining in the generation of turbidity maximum zones (TMZ), which are observed to extend for tens of kilometers along some shallow, open coastal seas. Idealized numerical simulations are conducted to reproduce the cross-shore dynamics and tidal straining in regions of freshwater influence (ROFIs), where elliptical current patterns are generated by the interaction between stratification and a tidal Kelvin wave. Model results show that tidal straining leads to cross-shore sediment convergence and the formation of a nearshore TMZ that is detached from the coastline. The subtidal landward sediment fluxes are created by asymmetries in vertical mixing between the stratifying and destratifying phases of the tidal cycle. This process is similar to the tidal straining mechanism that is observed in estuaries, except that in this case the convergence zone and TMZ are parallel to the shoreline and perpendicular to both the direction of the freshwater flux and the major axis of the tidal flow. We introduce the term minor axis tidal straining (MITS) to describe the tidal straining in these systems and to differentiate it from the tidal straining that occurs when the major axis of the tidal ellipse is aligned with the density gradient. The occurrence of tidal straining and the coastal TMZ is predicted in terms of the Simpson ( $Si$ ) and Stokes ( $Stk$ ) numbers, and top–bottom tidal ellipticity difference ( $\Delta\epsilon$ ). Based on our results, we find that  $SiStk^2 > 3$  and  $\Delta\epsilon > 0.5$  provide a limiting condition for the required density gradients and latitudes for the occurrence of MITS and the generation of a TMZ.

## 1. Introduction

Density stratification has a profound influence on circulation and sediment transport dynamics in estuaries

 Denotes content that is immediately available upon publication as open access.

*Corresponding author:* Raúl P. Flores, raul.flores@usm.cl

(Hansen and Rattray 1965; Burchard et al. 2013; Geyer and MacCready 2014) and in shallow coastal seas (Simpson et al. 1990; Stacey et al. 1999; Pietrzak et al. 2011). Riverine freshwater discharge strongly influences shallow coastal seas such as Liverpool Bay (Rippeth et al. 2001) and the Rhine River outflow region (Simpson and Souza 1995), which are often referred to as regions of freshwater influence (ROFIs; Simpson 1997). An important consequence of density

DOI: 10.1175/JPO-D-18-0264.1

© 2020 American Meteorological Society. For information regarding reuse of this content and general copyright information, consult the [AMS Copyright Policy \(www.ametsoc.org/PUBSReuseLicenses\)](https://www.ametsoc.org/PUBSReuseLicenses).

gradients in estuaries and ROFIs is the generation of subtidal residual landward sediment fluxes near the bed, which often lead to sediment convergence and regions of very high turbidity (Jay and Musiak 1994; Geyer et al. 2001; Burchard et al. 2013; Souza and Lane 2013). In this work we use an idealized numerical model to investigate the role of stratified tidal process in the generation of coastal turbidity maxima such as those observed in the Rhine ROFI (van der Hout et al. 2015).

In estuaries, turbidity maxima can be generated by several hydrodynamic and sediment transport processes (e.g., Geyer 1993; Burchard et al. 2018). A detailed review of such processes is given by Burchard et al. (2018) and includes gravitational (Burchard and Hetland 2010) and lateral (Lerczak and Geyer 2004; Nidzieko et al. 2009) circulation and tidal straining (Jay and Musiak 1994; Burchard et al. 2013, 2018). In some estuaries, subtidal landward sediment fluxes and the formation of estuarine turbidity maxima (ETM) have been attributed to tidal asymmetries in eddy viscosity generated by tidal straining (Jay and Musiak 1994; Scully and Friedrichs 2007). Tidal straining (Simpson et al. 1990) leads to a periodic cycle of stratification and destratification in which the water column becomes more mixed during flood tide. In the near-bed region, stronger mixing during the flood enhances landward currents relative to the ebb currents and results in upstream residual transport (Jay and Musiak 1994; Geyer et al. 2000; Scully and Friedrichs 2007).

Dynamics similar to those observed in estuaries frequently extend out onto the shelf in river plumes (Horner-Devine et al. 2015) and ROFI systems (Simpson 1997). Tidal straining along open coasts in ROFI systems results in periodic variations in stratification that control turbulence (Rippeth et al. 2001; Fisher et al. 2002; Souza et al. 2008; Fischer et al. 2009). Characteristic features of the tidal straining process in ROFI systems include a semidiurnal switching in water column stratification, cross-shore currents that are 180° out of phase between the surface and the bottom, and high tidal current ellipticities (e.g., Visser et al. 1994; Simpson and Souza 1995; de Boer et al. 2006; Palmer 2010). An example of the semidiurnal variations in stratification, current structure, and near-bed sediment transport induced by tidal straining is shown in Fig. 1 for a shallow site in the midfield region of Rhine ROFI (Flores et al. 2017; Horner-Devine et al. 2017). Although other processes, such as the propagation of tidal plume fronts (Horner-Devine et al. 2017; Rijnsburger et al. 2018), are also relevant in the midfield region, the main features of tidal straining are evident in the stratification and current time series (Figs. 1b,c); a strongly sheared alongshore (Fig. 1a) and cross-shore current profiles

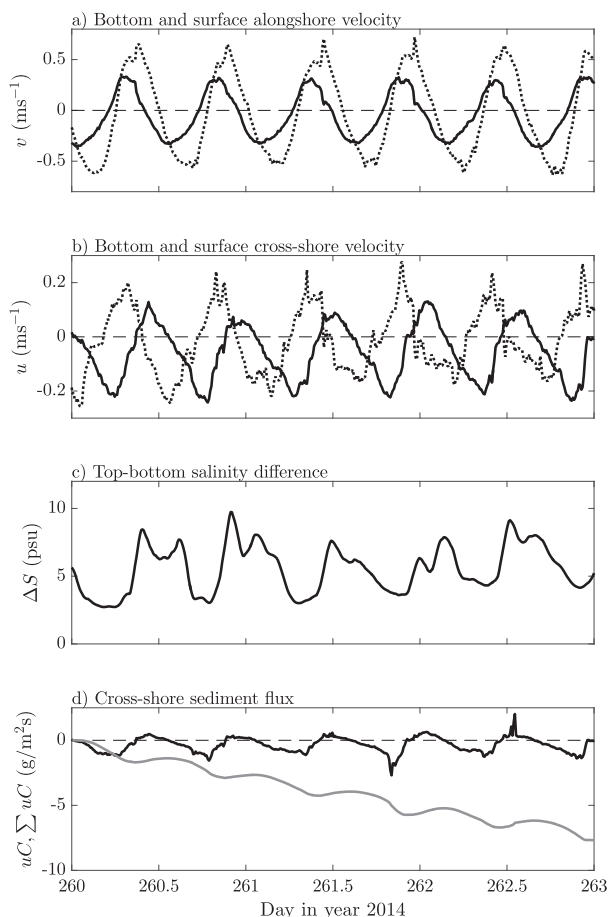


FIG. 1. Field measurements in the Rhine ROFI. (a) Bottom (solid line) and surface (dotted line) alongshore velocities. Positive velocities are directed to the northeast, and negative velocities are directed to the southwest. (b) Bottom (solid line) and surface (dotted line) cross-shore velocities. Positive velocities are directed offshore and negative velocities are directed onshore. (c) Top–bottom salinity difference. (d) Instantaneous (black line) and cumulative (gray line) near-bottom cross-shore sediment fluxes. Negative fluxes are directed onshore, and positive fluxes are directed offshore. These measurements were part of the Stratification Impacts on Nearshore Sediment (STRAINS) field campaign in 2014 and were taken 10 km north of the mouth of the Rhine River, in 18 m of water, approximately 5 km off the coast (Flores et al. 2017; Rijnsburger et al. 2018). These measurements were taken during neap tide and low wind conditions. In all panels, bottom refers to measurements collected approximately 2 m above the bed and surface refers to measurements collected 1 m below the surface. Suspended sediment concentrations were measured using optical backscatter (OBS). The reader is referred to Flores et al. (2017) for further details about the instrumentation and deployment.

(Fig. 1b) that result from the density differences (Fig. 1c) lead to a net landward transport of fine sediment at depth (Fig. 1d). The interplay between tides, density gradients, and bottom friction favors convergence processes that may lead to the formation of

turbidity maximum zones in ROFIs (e.g., Souza and Lane 2013; van der Hout et al. 2015; Brown et al. 2015; van der Hout et al. 2017). Yet the role of tidal straining in the generation of turbidity maximum zones in coastal regions has not been clearly established.

The occurrence of turbidity maximum zones (TMZs) is relevant for a wide variety of ecological processes and problems, as they are often related to the inhibition of primary production, hypoxia and the accumulation of contaminants (Eisma 1990; Yoshiyama and Sharp 2006). High concentration of suspended sediments can impair the optimal functioning of coastal engineering projects, which may then require unplanned modifications. The accumulation of fine sediments in estuarine waterways and coastal regions often requires further human intervention such as dredging. Thus, a better understanding of the physical processes that determine sediment pathways and accumulation zones is essential for coastal region management.

In the Rhine ROFI, a persistent turbidity maximum zone has been observed between 1 and 3 km from the coast (Fig. 2a), with peak sediment concentrations of 500–1000  $\text{mg l}^{-1}$  located approximately 1.25–1.5 km from the coast (van der Hout et al. 2015, 2017). Based on data collected during several measurement campaigns (e.g., van Alphen 1990; Joordens et al. 2001; van der Hout et al. 2015), this TMZ is thought to extend at least 80 km downstream of the mouth of the Rhine–Meuse estuary (Fig. 2b), making it the one of the main features of the fine sediment dynamics along the Dutch coast. As a result of vertical stratification, high suspended sediment concentrations are usually confined to the lower half of the water column (Fig. 2a) and are not detectable by remote sensing or satellite imagery (Pietrzak et al. 2011; van der Hout et al. 2015). The nearshore location of this TMZ is relevant for the coastal engineering solutions implemented along the Dutch coast in response to climate change and sea level rise (e.g., Stive et al. 2013), and it has also been shown to control the distribution of nutrients, plankton, and chlorophyll *a* in the coastal ecosystem (Joordens et al. 2001; van der Hout et al. 2017).

In stratified coastal regions where the tide behaves as a standing wave (e.g., Liverpool Bay; Rippeth et al. 2001; Palmer 2010), the major axis of the tidal currents is aligned with the horizontal density gradient and the tidal straining process is similar to that observed in estuaries. In coastal regions where the tide behaves as a progressive wave, such as the Rhine (Simpson et al. 1993), tidal currents are not aligned with the main horizontal density gradient. In this situation, tidal straining cannot occur without additional processes that align the tidal shear and the density gradients (Visser et al. 1994; Simpson

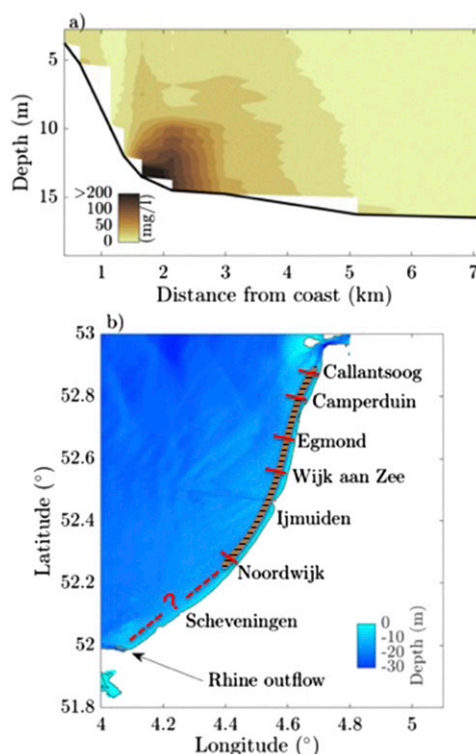


FIG. 2. Observation of a nearshore turbidity maximum zone along the Dutch coast. (a) Suspended sediment concentrations along a transect off the coast at Egmond [see (b)]. These measurements correspond to those of van der Hout et al. (2015). (b) Bathymetry along the Dutch coast. Red lines represent locations where a coastal TMZ was observed in the field measurements of van der Hout et al. (2015) and van Alphen (1990). The along-shore extension of the TMZ has been indicated by the brown filled area. The red dashed line indicates that the TMZ could potentially extend to the river mouth, although no measurements have been reported in that area.

and Souza 1995; Souza and Simpson 1996). Earth's rotation, which is often neglected in estuaries (Scully and Friedrichs 2007; Burchard et al. 2013), plays a key role in the generation of tidal straining in these ROFI systems by generating tidal shear parallel to the density gradient (Visser et al. 1994; Palmer 2010; Souza 2013).

Tidal straining in ROFIs with progressive tides is a frictional process that relies on the anticyclonic frictional boundary layer occupying the full water column (Visser et al. 1994; Simpson and Souza 1995). When the water column is strongly stratified, the eddy viscosity is reduced at the pycnocline and the top and bottom layers become dynamically decoupled (Visser et al. 1994; Verspecht et al. 2010; Palmer 2010). This decoupling leads to the modification of the tidal ellipses and the development of strong cross-shore velocity shear (Visser et al. 1994; Simpson and Souza 1995; Souza et al. 1997). As the upper layer does not feel bottom friction, it

develops strong anticyclonic rotation, which in turn enhances the cyclonic character of the near-bottom currents. The surface and bottom currents rotate in opposite directions, leading to the high cross-shore shear that results in the periodic cross-shore straining of the density field (Visser et al. 1994; Souza and James 1996; Palmer 2010; Souza 2013). Tidal current ellipticity (the ratio of semiminor to semimajor axes of the tidal ellipses) is used as a measure of tidal straining in ROFI systems (Visser et al. 1994; Souza et al. 1997; de Boer et al. 2006). In the Rhine, ellipticities approaching 0.4 have been observed in the field (Visser et al. 1994; Souza and Simpson 1996; Flores et al. 2017) and in numerical simulations (de Boer et al. 2006) during stratified conditions. De Boer et al. (2006) analyzed the elliptical structure of the tidal currents in the Rhine, concluding that the increase in current ellipticity is intrinsically tied to stratification within the plume.

Thus, tidal straining can occur in the direction of the major axis of the tidal flow, as in estuaries or coastal regions where the tide behaves as a standing wave, and/or in the direction of the minor axis of the tidal ellipse, as in coastal systems with progressive tides. We will refer to the tidal straining process that occurs in progressive wave ROFI systems as minor axis tidal straining (MITS) in order to differentiate them from the more common tidal straining process that occurs in estuaries and standing wave systems where the density gradient is aligned with the major axis of the tidal currents. We note that this term is not meant to describe a new phenomenon, as MITS has been extensively described in the literature over the years (Simpson et al. 1990; Visser et al. 1994; Simpson and Souza 1995; Verspecht et al. 2010). The term is introduced here in order to help differentiate the types of tidal straining in our discussion.

In this study, we focus on the impact of MITS on the cross-shore variability of suspended sediment transport dynamics and the generation of turbidity maximum zones in coastal regions. We use an idealized numerical model designed to reproduce the cross-shore circulation patterns set by the tidal straining mechanism, characteristic of ROFI systems with progressive tides. We test the hypothesis that tides and MITS result in the formation of a coastal turbidity maximum that is detached from the shoreline (as in Fig. 2) and investigate the mechanisms by which cross-shore sediment convergence is generated. The parameter space includes variations in the horizontal density gradient and the Coriolis parameter, which are thought to be the critical parameters governing tidal straining dynamics, as discussed in section 2, and sediment particle size (Rouse

number). Based on the results of our simulations, we provide a parameter space for the formation of TMZs and the occurrence of MITS in shallow coastal seas, specified in terms of nondimensional numbers controlling the buoyancy and frictional influence.

This paper is organized as follows: In section 2 we explore the scaling relationships that define the parameter space for MITS and define the major nondimensional numbers that are used throughout the paper. In section 3 we describe the numerical model, grid setup, simulation scenarios, parameters and forcing required to perform the hydrodynamic and sediment transport simulations. In section 4 we use model results to describe the processes leading to the formation of a TMZ for a base case scenario. In section 5 we discuss the mechanism that leads to cross-shore sediment convergence and investigate the parameter space for the generation of a TMZ by tidal straining, including the influence of particle size distributions. We present our final conclusions in section 6.

## 2. Nondimensional parameters

To develop a predictive understanding for the occurrence of MITS and turbidity maximum zones in coastal shelf seas we use nondimensional parameters that characterize tidal flows subjected to the influence of horizontal density gradients and Earth's rotation (Simpson et al. 1990; Monismith et al. 1996; Souza and Simpson 1996; Burchard et al. 2013; Souza 2013). The Simpson number ( $Si$ ) quantifies the relative influence of horizontal density gradients on the dynamics of estuarine and coastal flows (Simpson et al. 1990; Monismith et al. 1996; Stacey et al. 2010; Burchard et al. 2013; Geyer and MacCready 2014):

$$Si = -\frac{g}{\rho_0} \frac{\partial \rho}{\partial x} \frac{h^2}{u_*^2}, \quad (1)$$

where  $g$  is the gravitational acceleration,  $\rho_0$  is a reference density,  $\rho$  is density,  $H$  is water depth, and  $u_* = \sqrt{C_D}U$  is the friction velocity, where  $C_D$  is a drag coefficient and  $U$  is a tidal velocity scale. It is worth noting that the Simpson number corresponds essentially to the horizontal Richardson number ( $Ri_x$ ; e.g., Monismith et al. 1996; Stacey et al. 2001; Burchard and Hetland 2010), and represents the ratio of buoyancy input to mixing (Burchard and Hetland 2010; Burchard et al. 2013). For small values of  $Si$ , tidal mixing eliminates the stratification caused by tidal straining and baroclinic mean flows, whereas for large values of  $Si$  ( $Si \sim 1$ ) the water column will stratify (Monismith et al. 1996). For intermediate values of  $Si$ ,

strain-induced periodic stratification (SIPS) is expected to occur (Simpson et al. 1990).

The Stokes number (Stk) quantifies the relative importance of friction and inertia in oscillatory tidal flows (Stokes 1851; Prandle 1982; Baumert and Radach 1992; Winant 2007; Burchard and Schuttelaars 2012; Souza 2013), and is defined as the ratio of boundary layer height to total water depth,

$$\text{Stk} = \frac{\delta}{h}. \quad (2)$$

Souza (2013) used the Stokes number to explain frictional tidal dynamics and water column structure in the Irish Sea, concluding that  $\text{Stk} \sim 1$  is a good predictor for the location of tidal mixing fronts. A Stokes number  $\text{Stk} \geq 1$  means that the frictional layer is greater than the water depth, which in practical terms is interpreted as a boundary layer that covers the full water column.

ROFIs are frictional systems with strong rotational currents (Souza et al. 1997; de Boer et al. 2006). Earth's rotation is accounted for when estimating the frictional depth  $\delta$  by decomposing the tidal ellipses into cyclonic and anticyclonic rotational components (Godin 1972; Prandle 1982). Each component has a boundary layer thickness given by (Godin 1972; Prandle 1982; Soulsby 1983; Souza 2013)

$$\delta_{\pm} = \frac{C_0 u_*}{\omega \pm f}, \quad (3)$$

where  $C_0$  is a constant with value 0.075 (Soulsby 1983; Souza 2013),  $f$  is the Coriolis parameter, and  $\omega$  is the tidal frequency. In Eq. (3), the plus and minus signs are used to indicate the cyclonic and anticyclonic boundary layers, respectively. For the rest of this paper, we will use the anticyclonic Stokes number (Prandle 1982; Soulsby 1983; Souza 2013),

$$\text{Stk}_- = \frac{\delta}{h}, \quad (4)$$

which is computed by specifying the Coriolis frequency  $f$  at any given latitude and tidal velocity scale. For tidal ellipses to be modified by stratification, it is necessary that  $\text{Stk}_- \geq 1$ , that is, that the anticyclonic boundary layer reaches the surface (Souza 2013; Visser et al. 1994; Simpson and Souza 1995). In the presence of stratification (and reduction of eddy viscosity at the pycnocline),  $\text{Stk}_- \geq 1$  allows the surface layer to gain anticyclonic rotation, which is compensated by cyclonic rotation in the bottom layer leading to the development of counter rotating top and bottom tidal currents. If the

anticyclonic boundary layer does not reach the surface, the presence of stratification would not result in increased anticyclonic rotation in the upper layer as it would have already reached its free stream velocity under the tidal forcing. Thus,  $\text{Stk}_- \geq 1$  sets an important constraint on the occurrence of MITS and the generation of TMZs.

As pointed out earlier, in regions such as the Rhine and Liverpool Bay ROFIs, the interaction between the tidal shear and the horizontal density gradient results in tidal velocity profiles that deviate significantly from the otherwise rectilinear tidal flow (Visser et al. 1994; Palmer 2010). Hence, a third nondimensional parameter that is of dynamical interest in ROFIs is the tidal current ellipticity, and more specifically, the top–bottom ellipticity difference (Souza et al. 1997; de Boer et al. 2006)

$$\Delta\varepsilon = \varepsilon_b - \varepsilon_s. \quad (5)$$

In the presence of MITS,  $\Delta\varepsilon$  is a positive number, as the bottom layer has positive (cyclonic) rotation and the surface layer has negative (anticyclonic) rotation. Large values of  $\Delta\varepsilon$  are indicative of the development of strong counterrotating top and bottom cross-shore current components, while low values of  $\Delta\varepsilon$  are associated to the absence of MITS and a rectilinear alongshore tidal flow (Souza et al. 1997).

The occurrence of turbidity maximum regions is also conditioned to the particle size distribution of bed sediments. The influence of particle size and associated settling velocities is usually assessed in terms of the Rouse number (Rouse 1937; Hunt 1954), which describes the balance between particle settling and upward turbulent transport of sediment,

$$\text{Ro} = \frac{w_s}{\kappa u_*}, \quad (6)$$

where  $w_s$  is the particle settling velocity (constant),  $\kappa = 0.4$  is the von Kármán constant, and  $u_*$  is the friction velocity scale ( $u_* \sim \sqrt{C_D U}$ ).

### 3. Numerical model

We use the Regional Ocean Modeling System (ROMS) to simulate circulation and sediment transport dynamics in an idealized ROFI MITS system. ROMS is a three-dimensional, free-surface, primitive equation ocean model with a curvilinear orthogonal horizontal grid and a stretched terrain-following vertical grid. The model solves finite-difference approximations of the Reynolds-averaged Navier–Stokes equations using the Boussinesq and hydrostatic approximations

(Shchepetkin and McWilliams 2005; Warner et al. 2008b), and has been extensively used in idealized and realistic numerical simulations of shelf dynamics and associated transport processes (Harris et al. 2008; Warner et al. 2008a; Chen et al. 2013; Horwitz and Lentz 2014; Kumar et al. 2015). This section describes the model configuration and the physical parameters used in the numerical simulations.

The model is designed to reproduce the cross-shore hydrodynamic and sediment transport processes characteristic of systems with MITS, such as the Rhine ROFI. Early studies in the far field of the Rhine ROFI (Simpson and Souza 1995; Souza and James 1996) have suggested that the dynamics are, to a first-order, two-dimensional, with cross-shore variability in density and currents dominating over those in the alongshore direction. More recently, de Boer et al. (2008) showed that cross-shore straining is the dominant mechanism controlling the variability in water column stability and current structure in this region. Consequently, all of our analyses are focused on the cross-shore dynamics that may lead to the formation of a TMZ. The model setup does not resolve along coast variability or simulate processes that are characteristic of the near-field and mid-field river plume regions, such as the propagation of tidal plume fronts (Horner-Devine et al. 2017; Flores et al. 2017; Rijnsburger et al. 2018) and alongshore advection or straining (de Boer et al. 2008). While alongshore processes have implications for ROFI sediment transport, the simulations presented here focus on the simplest case in order to understand the fundamental processes that lead to cross-shore sediment convergence along this type of ROFI system.

### a. Model setup

The model domain consists of open ocean boundaries at the north, south and west boundaries and a coastal wall at the eastern boundary. The bathymetry is along-shore uniform, with a minimum depth at the coastal wall of  $h = 3$  (m) and maximum depth offshore of  $h = 30$  (m). We used an exponential fit that matches the steeper near shore slope of  $\alpha = 0.01$  and milder offshore slope of  $\alpha = 0.001$  observed in van der Hout et al. (2017) (Fig. 3a). The choice of a maximum depth of  $h = 30$  (m) is representative of the Rhine ROFI region along the southern North Sea (Pietrzak et al. 2011). The stretched vertical grid has  $N = 32$  levels with enhanced resolution in the near-bottom and near-surface regions (Fig. 3a).

To avoid boundary effects, the alongshore domain was set to 50 km with a resolution of  $\Delta y = 500$  (m), for a total of 100 grid cells. All of the analyses and figures presented here are from cross sections located in the

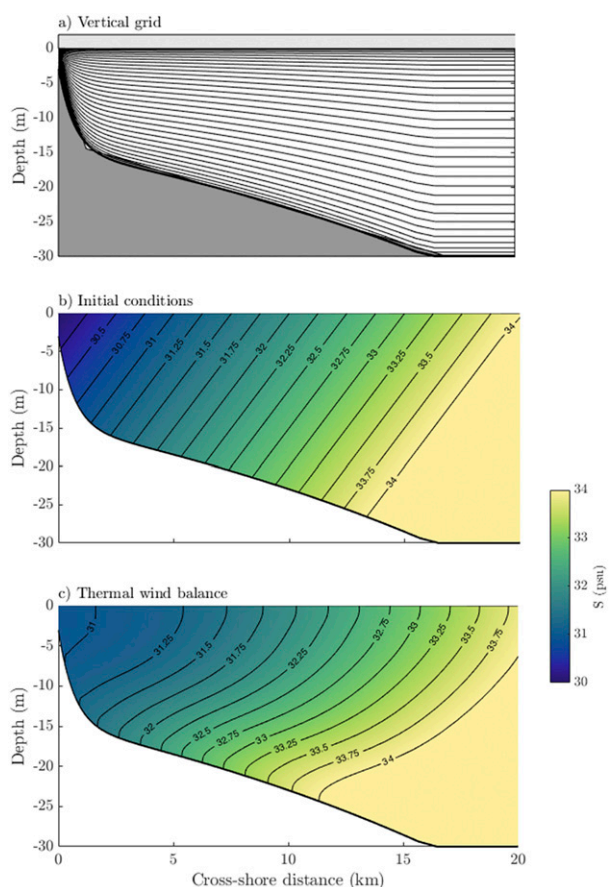


FIG. 3. (a) Model bathymetry and vertical terrain-following grid with near-surface and near-bottom increased vertical resolution. (b) Initial and (c) adjusted (due to thermal wind balance) salinity structure for the base case scenario. Only part of the cross-shore domain is shown.

middle of the domain ( $y = 25$  km). The tide is specified as a progressive Kelvin wave and, in order to let the Kelvin wave decay completely, the cross-shore domain spans 700 km but with variable grid resolution; grid size increases linearly from a minimum of  $\Delta x = 20$  m in regions adjacent to the coastal wall to a maximum of  $\Delta x = 5000$  m in offshore regions with flat bottom where dynamics are not of interest for this study.

Simulations are conducted following two steps; first, we let the system develop a thermal wind balance in response to an imposed depth-uniform cross-shore density gradient (Figs. 3b,c). Salinities and temperatures are then clamped at the thermal wind values at the northern boundary, in order to provide a constant buoyancy forcing that would result in the establishment of a bottom attached buoyant coastal current (Fig. 3c). Zero gradient boundary conditions are specified for the salinity, temperature, and suspended sediments at the southern and eastern boundaries. After the thermal

wind equilibrium has been reached and the buoyant coastal current has developed, we force the system with tidal elevations and velocities at each of the open boundaries, which are specified based on the expressions for a Kelvin wave with linear bottom friction (Jacobs 2004; de Boer et al. 2006; Roos et al. 2011). Chapman and Flather boundary conditions (Marchesiello et al. 2001) are used for the tidal elevation and depth-averaged velocities, respectively, at all the open boundaries.

In ROMS, the system of governing equations is closed using parameterizations of the Reynolds stresses in terms of eddy viscosities and eddy diffusivities. Eddy viscosities and eddy diffusivities were estimated using the  $\kappa$ - $\epsilon$  turbulence closure model (Umlauf and Burchard 2003; Warner et al. 2005). Background values for eddy viscosities and diffusivities are taken as  $K_v = 10^{-5} \text{ m}^2 \text{ s}^{-1}$  and  $K_s = 10^{-6} \text{ m}^2 \text{ s}^{-1}$ , respectively. Bottom stresses are determined using a logarithmic drag layer with a roughness length that results in a drag coefficient of approximately  $C_D = 0.003$ .

A detailed description of ROMS sediment transport module is provided elsewhere (Warner et al. 2008b), and the relevant sediment parameters are described below (section 3b). Model runs are initialized with zero concentrations in the water column, and since lateral sources of sediment were not specified at the boundaries, all the sediment in suspension in the model results from tidally induced erosion from the seabed. Boundary conditions for the sediment calculations are specified as zero gradient boundary conditions at all boundaries.

### b. Base case

The base case corresponds to typical neap tide conditions observed in the Rhine ROFI. Base case runs are initialized with a cross-shore uniform salinity gradient in the plume region of  $2 \times 10^{-4} \text{ psu m}^{-1}$ , which results in a depth-uniform cross-shore density gradient of approximately  $1.523 \times 10^{-4} \text{ kg m}^{-4}$ , representative of the far field region of the Rhine ROFI (Rijnsburger et al. 2016). Vertical stratification is imposed with a constant salinity gradient of  $0.05 \text{ psu m}^{-1}$  with a buoyancy frequency of  $N^2 = 1.2 \times 10^{-4} \text{ s}^{-2}$ . The width of the stratified region is set to 20 km, which is the typical cross-shore extension of the plume in the far field (Souza et al. 2008). As a result of the horizontal and vertical stratification, the isopycnals are initially diagonal as shown in Fig. 3b. The model is forced with semidiurnal tides with a frequency of  $\omega = 1.4054 \times 10^{-4} \text{ s}$  (M2 tidal constituent) and amplitude of  $\eta_0 = 0.8 \text{ m}$ , which is characteristic of neap tide along the Rhine region (Flores et al. 2017; Rijnsburger et al. 2018). The Coriolis parameter was set to  $f = 1.13 \times 10^{-4} \text{ s}^{-1}$ , corresponding to a latitude of  $51^\circ$ . No additional forcings such as wind or waves are included in the

simulations since our primary focus is the effect of MITS dynamics.

The sediment bed consists of one layer with two sediment classes, corresponding to fine silts ( $10 \mu\text{m}$ ) and fine sands ( $200 \mu\text{m}$ ). Settling velocities and critical stresses for erosion are  $0.1 \text{ mm s}^{-1}$  and  $0.05 \text{ Pa}$  for the fine fraction and  $1 \text{ cm}^{-1}$  and  $0.2 \text{ Pa}$  for the sand fraction. The erodibility constant is chosen to be  $5 \times 10^{-4} \text{ kg m}^{-2} \text{ s}^{-1}$  for both classes of sediment based on values reported by Sanford and Maa (2001). The bed is initialized with a silt fraction of 20% and a fine sand fraction of 80%, following observations along the Dutch Coast (Huisman et al. 2016; Flores et al. 2018).

### c. Numerical simulations

The parameters for the base case and nonbase case model runs used in this study are summarized in Tables 1 and 2. Horizontal density gradients range from  $3.81 \times 10^{-5}$  to  $2.3 \times 10^{-4} \text{ kg m}^{-4}$ , corresponding to salinity gradients ranging from  $5 \times 10^{-5}$  to  $3 \times 10^{-4} \text{ psu m}^{-1}$ . A case without stratification was also included in order to investigate whether a TMZ would form under well-mixed conditions. The Coriolis parameter was estimated as  $f = 2\Omega \sin(\psi)$ , where  $\Omega$  and  $\psi$  are the planetary rotation frequency and latitude, respectively, and was chosen to span latitudes from  $26^\circ$  to  $56^\circ$ . Parameters such as settling velocity, tidal range and water depth were also varied. To isolate the influence of the bathymetric profile from the overall depth, several runs were conducted using a bathymetric profile with a much smoother transition between shallow and deeper water and milder slopes (not shown). Model runs specified in Table 1 were performed using the bathymetric profile shown in Fig. 3, whereas the model runs specified in Table 2 were performed using the smoother profile. In Tables 1 and 2,  $\bar{H}$  refers to a mean water depth computed based on the bathymetric profile,

$$\bar{H} = \frac{1}{x_0} \int_0^{x_0} h(x) dx, \quad (7)$$

where  $x_0$  corresponds to the cross-shore extension of the initially stratified region,  $x_0 = 20 \text{ km}$ . To complete the parameter space with regard to the nondimensional number described in section 2, a small number of simulations were conducted with varying both density gradients and the Coriolis parameter.

## 4. Model results

### a. Density and current structure: MITS

The modeled velocity and salinity fields (Fig. 4) display periodic variations consistent with the characteristic



TABLE 1. Model runs.

Cases	Run	$\partial\rho/\partial x$ ( $10^{-4}$ kg m $^{-4}$ )	$f$ ( $10^{-4}$ s $^{-1}$ )	$\bar{H}$ (m)	$\eta_0$ (m)	$w_s$ (mm s $^{-1}$ )	Si	Stk $_c$
Base case	1	1.52	1.13	22.8	0.8	0.1	1.55	
Vary $\partial\rho/\partial x$	2	0	1.13	22.8	0.8	0.1	0	
	3	0.381					0.39	
	4	0.762					0.77	
	5	1.143					1.16	2.66
	6	1.714					1.75	
	7	1.910					1.94	
	8	2.09					2.12	
	9	2.28					2.33	
	Vary $f$	10	1.52	0.638	22.8	0.8	0.1	1.47
11			0.749				1.49	1.14
12			0.855				1.51	1.35
13			0.954				1.52	1.65
14			1.046				1.54	2.06
15			1.21				1.57	3.71
Vary $\eta_0$	16	1.52	1.13	22.8	0.6	0.1	1.78	1.88
	17				1.00		1.03	3.26
Vary $w_s$	18	1.52	1.13	22.8	0.8	0.05	1.55	2.66
	19					0.2		
	20					0.5		
	21					0.8		
	22					1		
	23	1.910	0.749	22.8	0.8	0.1	1.81	1.14
	24	1.714	0.855	22.8	0.8	0.1	1.69	1.35
	25	1.143	0.954	22.8	0.8	0.1	1.14	1.64
	26	0.762	0.855	22.8	0.8	0.1	0.76	1.35

variations in stratification and shear observed in ROFI systems with MITS described in section 1. The time series shown in Fig. 4 are for a time period where a quasi-steady state has been reached, several tidal cycles after the tides were initiated. In the Rhine, tides propagate as progressive Kelvin waves; positive alongshore velocities correspond to flood tide and

negative velocities correspond to ebb tide (Figs. 4a,b). The alongshore velocities are stronger during the flood, as the tidal flow and the density-driven circulation (thermal wind) act in the same direction. The cross-shore velocities are 180° out of phase between the surface and bottom (Figs. 4c,d), and show a marked two layer structure (Fig. 4c) indicative of the pycnocline at a depth of

TABLE 2. Model runs.

Cases	Run	$\partial\rho/\partial x$ ( $10^{-4}$ kg m $^{-4}$ )	$f$ ( $10^{-4}$ s $^{-1}$ )	$\bar{H}$ (m)	$\eta_0$ (m)	$w_s$ (mm s $^{-1}$ )	Si	Stk $_c$	
Vary $\partial\rho/\partial x$	27	0	1.13	17.6	0.8	0.1	0	3.53	
	28	0.381					0.22		
	29	0.762					0.45		
	30	1.143					0.68		
	31	1.52					0.911		
	32	1.714					1.023		
	33	1.910					1.14		
	34	2.28					1.25		
	Vary $f$	35	1.52	0.638	17.6	0.8	0.1	0.86	1.28
		36		0.749				0.88	1.49
37			0.855				0.89	1.77	
38			0.954				0.9	2.15	
39			1.046				0.9	2.7	
40			1.13				0.91	3.52	
41			1.21				0.92	4.88	
Vary $\eta_0$	42	1.52	1.13	17.6	0.6	0.1	1.56	2.65	
	43				1.00		0.61	4.28	

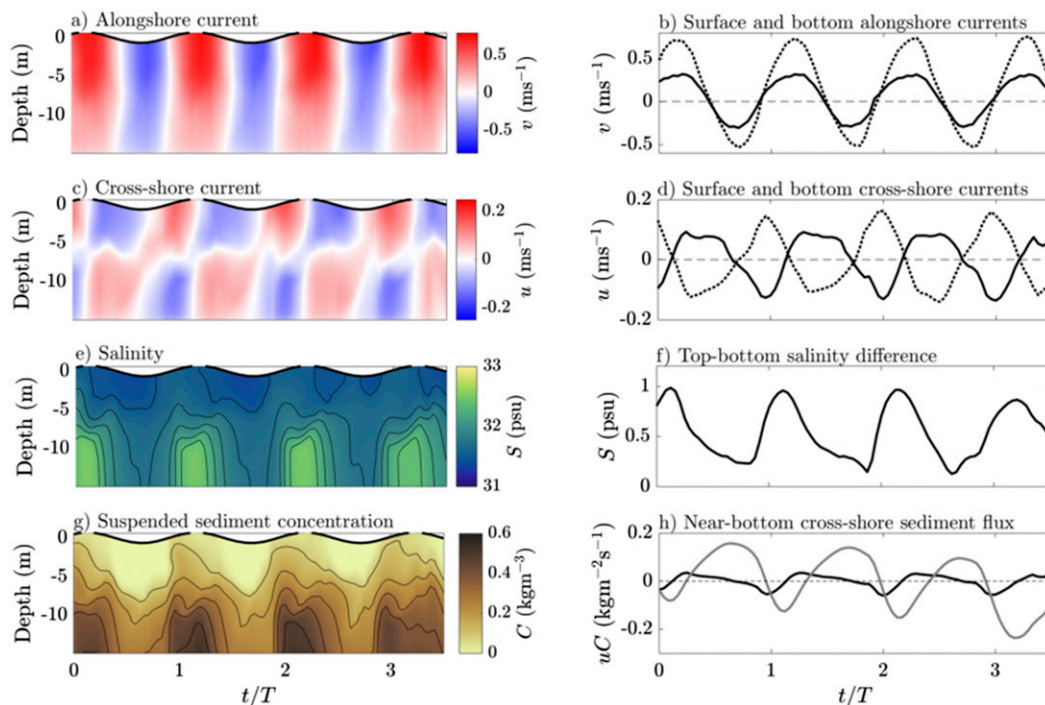


FIG. 4. MITS and sediment fluxes for the base case. (a) Alongshore current. (b) Time series of bottom (solid line) and surface (dashed line) alongshore current. (c) Cross-shore current. (d) Time series of bottom (solid line) and surface (dashed line) cross-shore current. (e) Salinity structure. (f) Time series of top–bottom salinity difference  $\Delta S$ . (g) Suspended sediment concentration. (h) Instantaneous (black line) and cumulative (gray line) near-bottom cross-shore fluxes. All panels show data corresponding to a site located in approximately 15 m of water. Positive alongshore current values correspond to the flood tide. Positive cross-shore current values correspond to offshore flow.

approximately 5 m below the surface. Maximum offshore and onshore velocities occur at slack tide, whereas minimum values occur at times close to peak ebb and peak flood tides. The cross-shore shear is on the order of  $0.2\text{--}0.3\text{ s}^{-1}$ , which is of similar magnitude as the vertical shear in the dominant alongshore currents (Figs. 4b,d).

The semidiurnal cycle of stratification and destratification is evident in the modeled fields shown in Fig. 4f, with maximum stratification occurring close to high water (peak flood) and minimum stratification at low water (peak ebb) as is characteristic of the Rhine ROFI (Simpson and Souza 1995; de Boer et al. 2006). The stratifying phase occurs from low water to high water (rising tide), whereas the destratifying phase occurs from high water to low water (falling tide) (Figs. 4b,f). Due to the progressive character of the tidal wave both phases include part of the ebb and flood tides. This differs from tidal straining in estuaries and ROFIs with standing tides where stratification increases during the ebb and decreases during flood (Simpson et al. 1990; Jay and Musiak 1994; Scully and Friedrichs 2007). Maximum and minimum top–bottom salinity

differences are on the order of 1 and 0.05 psu, respectively, suggesting that the water column almost reaches a completely well-mixed state during the peak ebb flow in 15 m of water (Fig. 4f).

The highest suspended sediment concentrations occur at times when the water column is stratified (Figs. 4e,g). Suspended sediment concentrations show a marked semidiurnal variability (Fig. 4g), indicating that the dynamics at this location are governed by horizontal advection. There is no clear evidence of a quarter-diurnal signal in the concentration, which is typically associated with local resuspension (Fig. 4g). We expect that the dominance of the advective (semidiurnal) over resuspension (quarter diurnal) variability in SSC is because the supply of fine erodible sediment is limited in the prescribed bed layer and the settling velocity is small. Thus, most of the fine bed layer is resuspended before the model achieves a quasi-steady state and stays in suspension for long periods of time. The cross-shore suspended sediment fluxes (Fig. 4h) show both onshore and offshore fluxes that occur during the stratifying and destratifying phases of the semidiurnal cycle, respectively. The net near-bed transport is

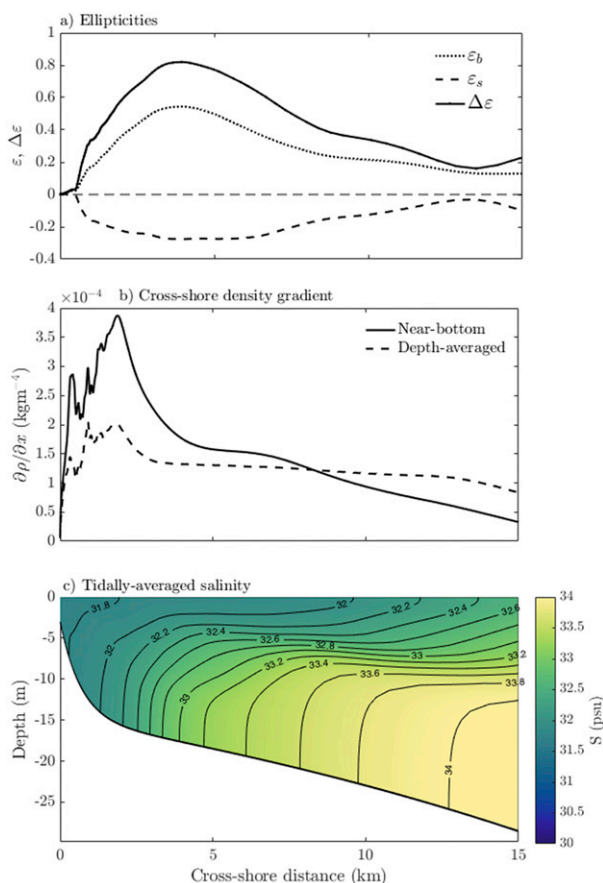


FIG. 5. (a) Near-bottom (dotted line) and near-surface (dashed line) tidal current ellipticity, and top–bottom ellipticity difference (solid line). (b) Near-bottom (solid line) and depth-averaged (dashed line) cross-shore density gradients. (c) Subtidal salinity structure.

landward (onshore) over the 3.5 tidal cycles shown in Fig. 4h (gray line). Further examination of the sediment fluxes and the mechanisms leading to subtidal transport is presented in section 4b.

Analysis of the velocity profile structure shows that the maximum ellipticity of the bottom and surface currents reach 0.5 and  $-0.3$ , respectively, leading to a maximum top–bottom ellipticity difference of  $\Delta\varepsilon \sim 0.8$  (Fig. 5a). These values are consistent with the field results of Visser et al. (1994) and Flores et al. (2017), both of which reported maximum  $\Delta\varepsilon$  of approximately 0.6–0.8, and the model results of de Boer et al. (2006) who reported ellipticities in the range from  $\varepsilon \sim -0.4$  to 0.5. Near-bed currents show greater ellipticity due to the concentration of frictional effects in the lower layer due to the presence of the pycnocline. Maximum tidal current ellipticities (surface and bottom) occur seaward of the region of maximum horizontal density gradient (Figs. 5a,b), in regions of

high vertical stratification. The tidally averaged salinity (Fig. 5c) has the structure of a bottom attached buoyant coastal current that is characteristic of shallow river plumes (Chapman and Lentz 1997; Geyer et al. 2004; Horner-Devine et al. 2015). On a subtidal time scale, we observe a two-layer salinity structure with a generally well-mixed bottom region as a result of the vertical mixing associated with the tidal currents, and a very stratified upper layer. This is consistent with previous modeling studies in the Rhine ROFI (Ruddick et al. 1995; de Boer et al. 2006).

The modeled density and current structure are thus consistent with the MITS observed in the far field of the Rhine ROFI (Visser et al. 1994; Simpson and Souza 1995; Simpson 1997). We note that our model was setup to be representative of the far-field ROFI dynamics, and thus is expected to only qualitatively reproduce the main features of the field data shown in Fig. 1, which are from the midfield region. Several additional processes occur in the midfield region that do not occur in the far field and are not included in our idealized model, including the propagation of tidal plume fronts (Rijnsburger et al. 2018) and alongshore advection (de Boer et al. 2008). A comparison between Figs. 1 and 4 suggests that the model qualitatively captures the main dynamical features observed in the field data, such as the semidiurnal switching in stratification, counter rotating top–bottom tidal currents and onshore suspended sediment fluxes. Furthermore, similar qualitative agreement is also present in comparison with other field data collected in the far field (e.g., Visser et al. 1994; not shown), such that both the field observations and our model results show surface and bottom alongshore currents that are in phase, and surface and bottom cross-shore currents that are  $180^\circ$  out of phase, resulting in similar counterrotating tidal currents and top–bottom ellipticity differences.

#### b. Turbidity maximum zone and sediment fluxes

The main objective of this modeling study is to investigate whether MITS leads to cross-shore sediment convergence and the formation of a coastal turbidity maximum zone (e.g., Fig. 2a). For comparison, we also show the response of the system for the unstratified case. Suspended sediment concentrations for run 2 (see Table 1) clearly indicate the absence of a localized turbidity maximum zone, although suspended sediment concentrations are generally high in nearshore regions (Fig. 6b). Without stratification, suspended sediments are mixed over the entire water column and typical Rouse profiles are observed throughout the domain (Figs. 6e,f). Suspended sediment concentrations are greater near the shore as a result of enhanced

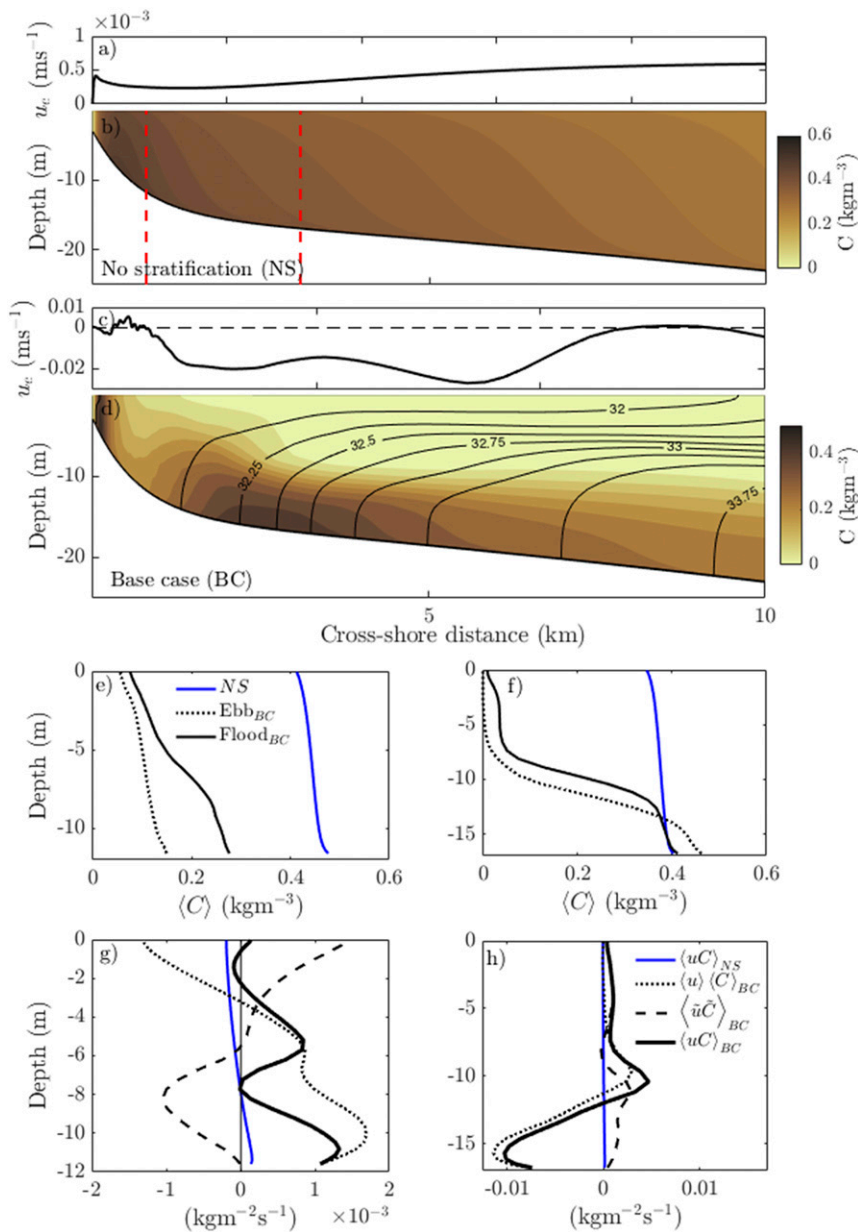


FIG. 6. (a) Near-bed effective transport velocity [Eq. (9)] for the no stratification (NS) case. (b) Tidally averaged suspended sediment concentrations for the no stratification case. (c) Near-bed effective transport velocity for the base case (BC). (d) Tidally averaged suspended sediment concentrations for the base case. (e) Ebb (dotted lines) and flood (solid lines) suspended sediment concentration profile at a cross-shore section indicated by the leftmost vertical red dashed line in (b). Blue indicates concentration for the no stratification case, and black indicates concentrations for the base case. (f) As in (e), but at a cross-shore location indicated by the rightmost vertical red dashed line in (b). (g) Residual transport components at the cross-shore location indicated by the leftmost red dashed line in (b). Blue indicates values for the no stratification case, and black indicates values for the base case. (h) As in (g), but at a cross-shore location indicated by the rightmost red dashed vertical line in (b).

sediment resuspension, and maximum depth-averaged concentrations occur at water depths of 5–8 m (Fig. 6b). From this, two important inferences can be made; first, bed stress resulting from the tidal currents is

large enough to erode the seabed and resuspend fine sediments, and second, we do not observe asymmetries between the flood and ebb phases of the tide (Figs. 6e,f).

The flow is significantly different for the stratified case (base case, run 1; Fig. 6d). The combination of MITS dynamics with a tidal flow capable of resuspending fine sediments (as shown in Figs. 4 and 5) results in the formation of a nearshore TMZ. A localized region with high suspended sediment concentrations extends between 1.5 and 4 km from the coast and in water depths greater than 12 m. Due to vertical stratification, the TMZ is confined to the near-bed region. The location and extension of the TMZ is remarkably similar to the observations reported by van der Hout et al. (2015) (Fig. 2a). The landward limit of the TMZ corresponds well with the tidally averaged position of the salinity (density) front (Fig. 4c) and the maximum near-bed horizontal density gradient (Fig. 4b). The overall extension and position of the TMZ is well predicted by the regions of high tidal current ellipticity, particularly that of the near-bed currents,  $\varepsilon_b \geq 0.5$  (Figs. 5a and 6d).

### 1) SUBTIDAL SEDIMENT FLUXES AND EFFECTIVE TRANSPORT VELOCITY

To investigate the mechanisms that lead to sediment convergence and the generation of the TMZ, we decompose the residual cross-shore sediment flux into contributions from the residual tidal current and the tidal fluctuations (Burchard et al. 2008; Schulz and Umlauf 2016),

$$\langle uC \rangle = \langle u \rangle \langle C \rangle + \langle \tilde{u}\tilde{C} \rangle, \quad (8)$$

where  $u$  is the cross-shore velocity,  $C$  is the suspended sediment concentration,  $\tilde{u} = u - \langle u \rangle$ ,  $\tilde{C} = C - \langle C \rangle$ , and the brackets denote the tidal averaging operator  $\langle u \rangle = (1/T) \int_0^T u dt$ , where  $T$  is the tidal period. The first term on the right-hand side of Eq. (8) represents the contribution from the residual currents to the total subtidal transport, whereas the second term represents the contribution from the covariance between the cross-shore velocity and sediment concentration. This last term is usually referred to as tidal pumping (Scully and Friedrichs 2007). Dividing Eq. (8) by the tidally averaged sediment concentration  $\langle C \rangle$  gives a quantity that can be interpreted as an effective cross-isobath sediment transport velocity (Schulz and Umlauf 2016),

$$u_e = \langle u \rangle + \frac{\langle \tilde{u}\tilde{C} \rangle}{\langle C \rangle}. \quad (9)$$

The base case  $u_e$  is at least an order of magnitude greater than that obtained for the unstratified scenario (Figs. 6a,c). Since suspended sediment concentrations are of similar magnitude in both scenarios, the difference in the magnitude of  $u_e$  is explained by the differences in the cross-shore flow. Under well-mixed

conditions, the Kelvin wave velocities are not modified and the flow is predominantly coast parallel, whereas in the presence of stratification, MITS generates strong cross-shore currents (Figs. 4d and 5a). Differences in direction of transport are also observed between these two cases;  $u_e$  is directed offshore (positive) for the unstratified case whereas  $u_e$  is predominantly onshore (negative) for the stratified case. For the stratified case, however, a transition from onshore to offshore transport is observed in water depths of approximately 15 m. This creates a region of transport convergence that is collocated with the landward limit of the turbidity maximum zone (Figs. 6c,d). Toward the coast, a region of transport divergence (transition from onshore to offshore) explains the relatively lower suspended sediment concentrations observed in intermediate water depths (6–12 m).

Individual terms contributing to the residual transport  $\langle uC \rangle$  at two cross-shore locations are shown in Figs. 6g and 6h. Contributions from the residual current dominate the residual sediment flux at both locations, and, since the direction of these fluxes is opposite, it creates the convergence region where suspended sediments preferentially accumulate. The covariance flux  $\langle \tilde{u}\tilde{C} \rangle$  generally opposes the fluxes driven by the residual current at both locations and is relatively more important at the shallower location. Notable differences in magnitude exist between the stratified and well-mixed cases, as could be expected from the magnitudes observed for  $u_e$  (Figs. 6a,c).

### 2) MECHANISM OF FORMATION OF THE TMZ

To examine the drivers for net landward residual transport, the water column structure over two tidal cycles and subtidal profiles of salinity, eddy viscosity, suspended sediment concentrations, cross-shore velocities, and cross-shore sediment fluxes are considered at a cross-shore location in 17 m of water within the TMZ (Fig. 7). The subtidal profiles have been averaged over the rising and falling phases of the tidal cycle, rather than over flood and ebb tides, to analyze the effect of MITS. During the rising phase the overall water column is becoming more stratified, whereas during the falling phase the water column becomes less stratified (Figs. 4e,f). The water column remains stratified at this site during both phases (Figs. 7a,b). However, the lower layer, within 5 m of the bottom, is well mixed during the rising tide phase whereas it is more stratified during the falling tide phase (Fig. 7b).

The sequence of stratification and mixing near the bed is somewhat counterintuitive as the phasing is different from tidal straining in estuaries, where higher eddy viscosity values occur during the destratifying part of the

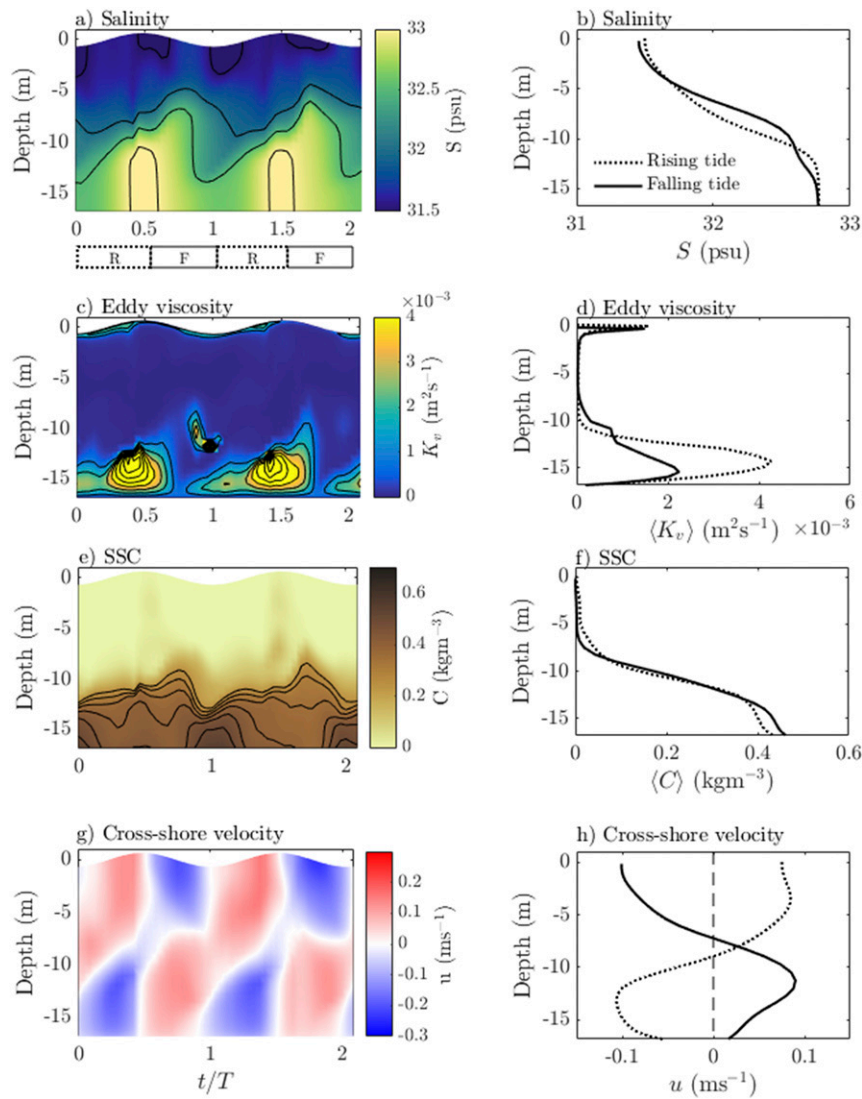


FIG. 7. (a) Salinity structure. The bar along the  $x$  axis indicates the rising tide and falling tide periods. (b) Mean salinity profiles for the rising tide (dotted line) and falling tide (solid line) phases of the tidal cycle. (c) Eddy viscosity. (d) Mean eddy viscosity profiles for the rising tide (dotted line) and falling tide (solid line) phases of the tidal cycle. (e) Suspended sediment concentrations. (f) Suspended sediment concentrations profiles for the rising tide (dotted line) and falling tide (solid line) phases of the tidal cycle. (g) Cross-shore velocity. (h) Cross-shore velocity profiles for the rising tide (dotted line) and falling tide (solid line) phases of the tidal cycle.

tidal cycle (Jay and Musiak 1994). Like estuaries, mixing occurs in near-bottom waters when saltwater is transported landward, resulting in elevated eddy viscosity near the bottom. Due to the counter rotation of top and bottom currents in the MITS system, however, this process occurs during the rising tide, when tidal straining generates higher top–bottom stratification in the water column. Thus, higher eddy viscosity occurs near-bottom when the overall water column is becoming more stratified (Figs. 7a,d). During the falling phase of the tide we observe that the overall water column

stratification decreases; however, the bottom layer remains stratified (Fig. 7b) leading to a reduction in the eddy viscosity (Fig. 7d). Near the bed, the asymmetry in eddy viscosity results in larger onshore directed cross-shore velocities during the rising tide phase compared with the magnitude of the offshore velocity during the falling tide phase (Fig. 7h). The net result is a landward subtidal current near the bed.

Suspended sediments are confined to the lower layer and no significant differences in sediment concentration exist between the rising tide and falling tide phases

(Figs. 7e,f). This observation is consistent with the fact that resuspension is limited by the availability of erodible bed sediments and thus there is no additional source of sediment on either tidal phase. Thus, the landward subtidal sediment fluxes in 17 m of water (Fig. 6h) are predominantly driven by the asymmetries in the residual cross-shore velocity rather than by asymmetries in the suspended sediment concentrations.

The results above suggest that the subtidal landward sediment fluxes are driven by asymmetries in vertical mixing near the bed that result from the stratification cycle created by the MITS dynamics. The cross-shore variability in eddy viscosity asymmetry is shown in Fig. 8, along with the structure of the subtidal cross-shore and alongshore transports. The asymmetry in eddy viscosity is obtained as  $|\Delta K_v| = |K_{v,r} - K_{v,f}|$ , where  $K_{v,r}$  and  $K_{v,f}$  correspond to the mean values of eddy viscosity over the rising tide and falling tide phases, respectively. The structure of  $|\Delta K_v|$  explains the subtidal cross-shore transport structure (Fig. 8b) and the overall location of the TMZ. The largest values of  $|\Delta K_v|$  occur in water depths between 12 and 20 m (Fig. 8a), which coincides with regions of elevated landward near-bed transport (Fig. 8b). The change in the direction of transport that occurs in water depths of approximately 15 m is collocated with the location where  $|\Delta K_v|$  significantly increases in the offshore direction (Figs. 8a,b), and also coincides with the tidally averaged position of the salinity (density) front (Figs. 4b,c). The strong correlation between  $|\Delta K_v|$ , the subtidal cross-shore transport and the location of the TMZ support the conclusion that the processes governing the generation of the TMZ are controlled by the effects of mixing asymmetries on the residual velocity profiles.

The alongshore subtidal transport is shown in Fig. 8c for completeness. Alongshore fluxes are generally higher than the cross-shore fluxes, with northward transport nearshore in the coastal current and southward transport farther offshore. The shear in the alongshore current is centered at the location of the maximum cross-shore density gradient in the middle of the TMZ and coincides with the region of highest  $|\Delta K_v|$  (Figs. 8a,c). The net residual transport within the TMZ is directed toward the north (positive) due to the stronger flow within the buoyant coastal current, though the net flux to the south is also substantial.

### 3) INFLUENCE OF THE HORIZONTAL DENSITY GRADIENT

The magnitude of the horizontal density gradient is expected to have a direct impact on the occurrence, magnitude, and location of the TMZ. Figure 9 shows

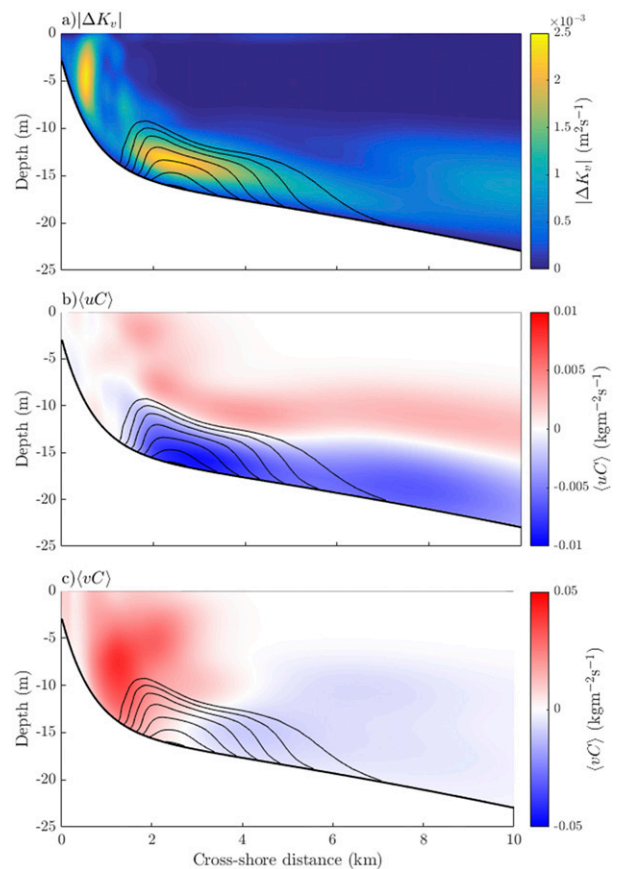


FIG. 8. (a) Cross-shore structure of the asymmetries in eddy viscosity  $|\Delta K_v|$  (see text for definition). (b) Cross-shore residual sediment transport. Negative values correspond to onshore transport, positive values correspond to offshore transport. (c) Alongshore residual transport. Positive values correspond to northward transport and negative values correspond to southward transport. In all panels, the contour lines correspond to the suspended sediment concentrations within the TMZ.

the effective transport velocity  $u_e$  and suspended sediment concentrations as a function of the initial horizontal density gradient for model runs 1–9 (see Table 1). Results are shown in terms of a normalized cross-shore coordinate  $x/W$ , where  $W$  is the initial width of the stratified region ( $\sim 20$  km). Regions of transport convergence (transition from  $u_e > 0$  to  $u_e < 0$ ) are evident (Fig. 9a), and correlate well with regions of high suspended sediment concentrations (Fig. 9b). The TMZ is the region of elevated sediment concentrations that is detached from the coast. Our results show that the landward limit of the TMZ is set by the region of transport convergence and that the TMZ only occurs for initial density gradients greater than approximately  $10^{-4} \text{ kg m}^{-4}$ . We find that the landward limit of the TMZ moves slightly onshore as the initial density gradient increases (Fig. 9b), however, not

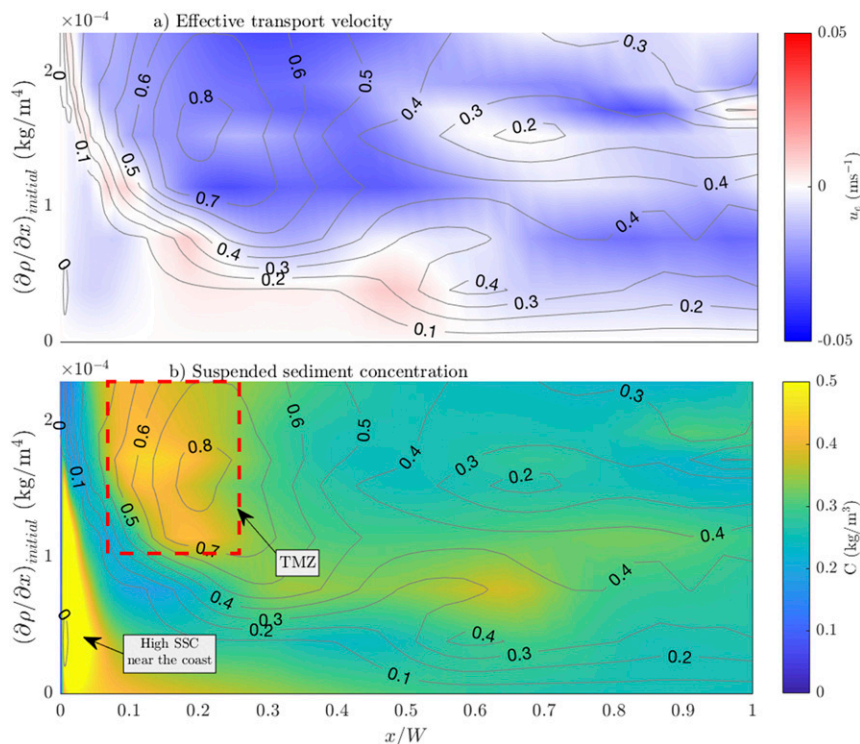


FIG. 9. (a) Effective transport velocity. Contour lines represent top–bottom ellipticity difference  $\Delta\epsilon$ . (b) Vertically averaged suspended sediment concentrations over the bottom 1 m. Contour lines represent top–bottom ellipticity difference  $\Delta\epsilon$ . The  $x$  axis in (a) and (b) represents cross-shore distance normalized by the width of the stratified region (20 km). The  $y$  axis represents the horizontal density gradient used to initialize model runs.

much variation is observed for initial density gradients greater than  $1.5 \times 10^{-4} \text{ kg m}^{-4}$ .

The TMZ is always observed in regions with large values of the top–bottom ellipticity difference (Fig. 9). Typically, the TMZ occurs in regions where  $\Delta\epsilon > 0.5$ , which occur for large values of the initial horizontal density gradient. It should be noted that high concentrations are also observed in shallow waters ( $x/W < 0.1$ ), but these are not attributed to MITS since they occur in a well-mixed water column with  $\Delta\epsilon \sim 0$  (Fig. 9b).

## 5. Discussion

### a. Mechanism of formation of the TMZ

Our model results show that the TMZ only forms when tidal ellipticity and cross-shore tidal currents are high, linking it clearly to the occurrence of MITS (Fig. 9). Stratification alone, without the ellipticity generated by MITS (low values of  $\Delta\epsilon$ ), does not result in the formation of a TMZ in intermediate water depths (runs 3, 4, 28, 29). This was further confirmed in model simulations in which tidal amplitude  $\eta_0$  was significantly decreased and no TMZ

formed (not shown). Reducing tidal amplitude leads to a decrease in tidal velocities, which in turn limits the magnitude of the cross-shore velocities and cross-shore straining. This suggests that the existence of a horizontal density gradient alone is not enough to generate a TMZ, and that moderate to high tidal flow velocities are needed in order to generate the convergence in transport.

The mechanism leading to sediment flux convergence in ROFI systems with progressive tides (MITS) described in the present work is very similar to the tidal straining mechanism in estuaries that leads to the formation of estuarine turbidity maxima (Jay and Musiak 1994; Scully and Friedrichs 2007). In both processes, landward sediment fluxes are generated by tidal asymmetry in the eddy viscosity and current structure. The processes differ in terms of the orientation and phasing with the tides. In estuaries the tidal flow is aligned with the density gradient. In MITS, the dominant component of the tidal flow is perpendicular to the density gradient and straining only comes about due to cross-shore motion associated with the tidal ellipticity. The phasing is also different between MITS and tidal straining in



estuaries. In estuaries, more near-bed mixing is generated during the destratifying phase of the tidal cycle on flood tide than occurs during the stratifying phase on ebb tide (Jay and Musiak 1994; Burchard et al. 2013). As discussed in section 4b(2), we find that MITS leads to enhanced mixing and a well-mixed region near the bed during the stratifying phase of the semidiurnal cycle, which corresponds to the transition between low water and high water (rising tide phase). These results are consistent with previous studies that investigated the effects of MITS on the cycle of turbulence and TKE dissipation in the Rhine system (Fisher et al. 2002; Souza et al. 2008; Fischer et al. 2009). Souza et al. (2008) found that the effect of MITS is to create instability in the water column as the cross-shore shear forces denser, higher-salinity water over fresher water. They hypothesized that the potential energy released by the straining mechanism leads to convective motions and enhanced turbulence near the bed. Similarly, Fischer et al. (2009) showed that unstable stratification develops near the bottom during the low to high water transition, with negative Richardson number and buoyancy frequency, which is indicative of mixing due to shear instabilities. In agreement with this, we find higher values for the eddy viscosity during the rising tide phase of the semidiurnal cycle, in which near-bed velocities are directed on-shore and thus force denser water over fresher less dense water.

In addition to the important role of the cross-shore density gradient, Earth's rotation and progressive tides are both necessary conditions for MITS. Earth's rotation sets the thickness of the cyclonic and anticyclonic boundary layers, which lead to the modification of the predominantly alongshore progressive tidal flow in the presence of stratification. As shown in section 4b, the fact that cross-shore straining occurs in systems with progressive tides can lead to the formation of turbidity maximum zones over long stretches of coast (e.g., Fig. 2). Coastal regions with progressive tidal waves can be frequently found at mid latitudes, for which  $\delta_- \gg \delta_+$ , suggesting that MITS and coastal TMZs, such as the one observed in the Rhine (van der Hout et al. 2015), may occur in other river plume systems. For example, progressive tidal waves are observed in the East China Sea (Wu et al. 2014) and along the Scottish and English coast in the North Sea (Huthnance 1991).

#### b. The role of water depth and bed slope on the location of the TMZ

In this section we use our model results to investigate the roles of water depth and bed slope as factors in the cross-shore location of the TMZ. Figure 10 shows near-bed suspended sediment concentrations for five

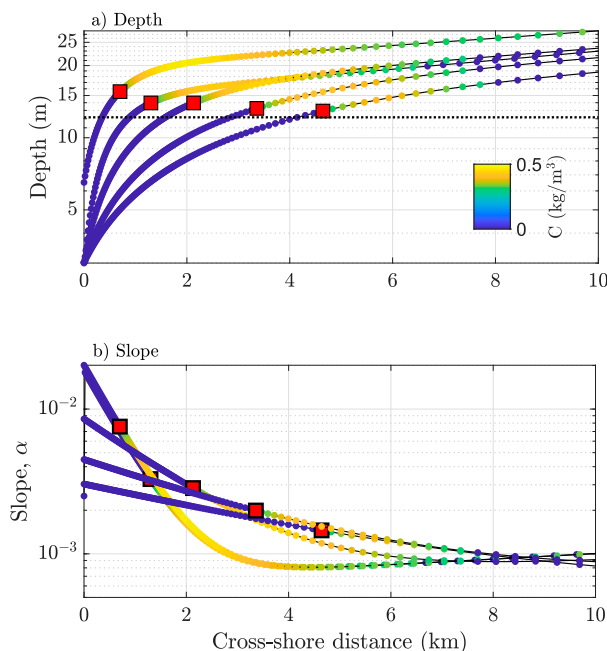


FIG. 10. Depth/slope dependence. (a) Water depth as a function of cross-shore distance for five bathymetric profiles. The color bar indicates suspended sediment concentrations in the TMZ. High suspended sediment concentrations near the coast have been removed for clarity. Red squares indicate the landward limit of the TMZ ( $0.3 \text{ kg m}^{-3}$  contour). The dashed horizontal line indicates the Simpson et al. (1990) SIPS limit for the horizontal density gradient and tidal velocity used in these simulations. (b) Bottom slope as a function of cross-shore distance for the five bathymetric profiles shown in (a). The color bar indicates suspended sediment concentrations in the TMZ. High suspended sediment concentrations near the coast have been removed for clarity. Red squares indicate the landward limit of the TMZ ( $0.3 \text{ kg m}^{-3}$  contour).

different bathymetric profiles tested in our numerical simulations, which spanned a wide range of water depths (Fig. 10a) and bed slopes (Fig. 10b). For clarity, in Fig. 10 we have masked the high suspended sediment concentrations in the nearshore, which are not a consequence of MITS. Figure 10a shows that the landward limit of the TMZ is located at similar water depths ( $h \sim 12\text{--}15 \text{ m}$ ), whereas Fig. 10b shows that the landward limit of the TMZ occurs at bed slopes spanning an order of magnitude. This suggests that the location of the TMZ is controlled by water depth rather than by a limiting bed slope value. We also tested whether the change in slope ( $da/dx$ ) influenced the location of the TMZ but did not find a meaningful relationship (not shown).

We use potential energy anomaly arguments (e.g., Simpson et al. 1990; Rippeth et al. 2001) to further investigate the dependence of the location of the TMZ on water depth. Simpson et al. (1990) proposed a limiting condition for the occurrence of SIPS (strain-induced

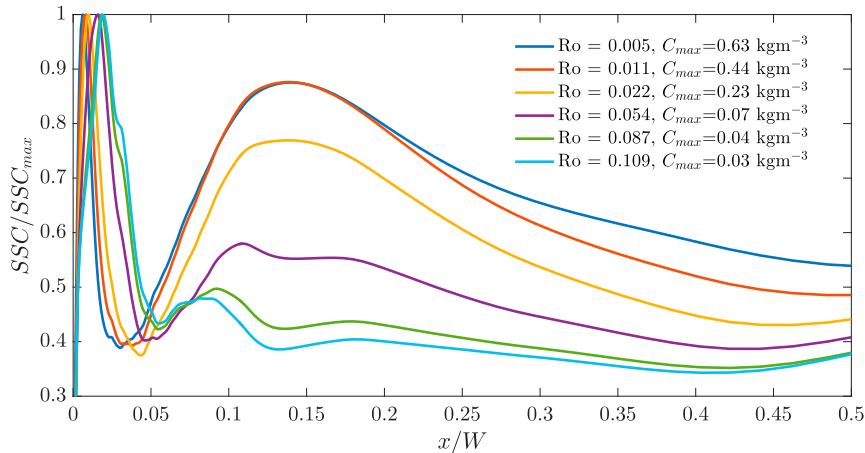


FIG. 11. Normalized suspended sediment concentrations as a function of the Rouse number. Values of the Rouse numbers and maximum concentrations observed in the TMZ are given in the legend. The  $x$  axis corresponds to cross-shore distance normalized by the initial width of the stratified region (20 km).

periodic stratification) based on the contribution of tidal straining to the total potential energy anomaly

$$\frac{1}{\rho} \frac{\partial \rho}{\partial x} \geq 2.2 \times 10^{-5} \left( \frac{u}{h} \right)^2, \quad (10)$$

where  $u$  is tidal velocity,  $h$  is water depth, and  $\partial \rho / \partial x$  is the depth-uniform cross-shore density gradient. Equation (10) can then be used to obtain a limiting water depth value for the occurrence of SIPS given a density gradient and a tidal velocity scale; at water depths greater than the limit provided by the SIPS condition the water column will show periodic stratification, whereas if water depth is less than the SIPS condition the tidal energy is sufficient to mix the water column, preventing the occurrence of SIPS and tidal straining. For the values used in our model simulations, the SIPS limit is exceeded only when  $h \geq 12.5$  m, which is consistent with the results shown in Fig. 10a. This limiting depth value sets the location of the cross-shore salinity front and the region of strong intratidal eddy viscosity variations that supports the formation of the TMZ (Fig. 7). Thus, we hypothesize that the location of the TMZ is set by water depth rather than by bottom slope, and that the TMZ will occur only at water depths greater than the limit provided by the SIPS condition.

### c. Influence of particle size and Rouse number

The occurrence of turbidity maximum zones is conditioned to the particle size distribution of bed sediments since only fine sediment particles are able to stay in suspension for long periods of time and be transported as suspended load. We have restricted model

simulations to very fine particles; the bed is predominantly sandy but includes 20% of medium to fine silts with varying settling velocities in the range from  $\sim 0.1$ – $1 \text{ mm s}^{-1}$ .

The cross-shore distribution of suspended sediment concentrations for different Rouse numbers (runs 18–22, Table 1) are shown in Fig. 11. The Rouse number is computed using the settling velocity of the fine sediment fraction. Suspended sediment concentrations have been normalized by the maximum observed concentrations to highlight the spatial variability. The coastal TMZ is identified as the second peak in the cross-shore distribution of suspended sediment concentrations (around  $x/W \sim 0.1$ ) and exists for all Rouse numbers in our range. As discussed in section 4, the very nearshore peak in the distribution of suspended sediment concentration occurs in very shallow waters and does not result from MITS dynamics. The suspended sediment concentrations decrease as the Rouse number (or settling velocity) increases because the tidal forcing and thus bottom stresses were kept fixed in these simulations. Peak suspended sediment concentrations in the TMZ range from  $C_{\max} = 0.03 \text{ kg m}^{-3}$  to  $C_{\max} = 0.63 \text{ kg m}^{-3}$ , corresponding to the maximum and minimum Rouse numbers, respectively. We find that as the Rouse number increases, the cross-shore extension of the TMZ becomes narrower, and the TMZ peak concentrations approach the background concentrations (Fig. 11).

Since the hydrodynamics of the simulations shown in Fig. 11 were kept the same (tidal forcing and stratification), we conclude that the characteristics of the TMZ rely heavily on the particle size distribution of bed sediments. In our simulations we have simplified the

sediment dynamics by including only one class of fine sediments. A more realistic particle size distribution may alter the cross-shore distribution of suspended sediment concentration, as the magnitude of the residual and covariance sediment fluxes are affected by particle size (Schulz and Umlauf 2016; Burchard et al. 2013). In this study, the subtidal sediment flux is always dominated by the tidal residual component, independent of the settling velocity of bed sediments (not shown). However, the covariance fluxes in the near-bed region do become more important as settling velocity increases, suggesting that a larger distribution of particle sizes may modify the size and concentration of the TMZ. Despite this, we do not expect that including more complex particle size distributions would affect the conclusions obtained with respect to the mechanisms of formation of the TMZ.

We note that the results presented above regarding the effects of particle size suggest that the existence of the TMZ is conditioned on the presence of fine sediments, which in reality is likely to vary seasonally. In fact, van der Hout et al. (2015, 2017) reported on seasonal variations in SPM concentrations within the TMZ along the Rhine ROFI, with clear differences between winter and summer. While it is likely that the TMZ never disappears completely, both observations and our modeling results support the idea that the TMZ may be seasonally ephemeral and conditioned on fine sediment availability.

#### d. The parameter space of MITS and the TMZ

The occurrence of a coastal TMZ and MITS is analyzed in terms of the nondimensional parameters described in section 2, the Simpson number ( $Si$ ; or horizontal Richardson number), the anticyclonic Stokes number ( $Stk_-$ ), and the top–bottom ellipticity difference ( $\Delta\varepsilon$ ). Combining  $Si$  and  $Stk_-$  [Eqs. (1) and (4)] results in

$$SiStk_-^2 = \frac{g \partial \rho}{\rho \partial x} \frac{C_0^2}{(\omega - f)^2}. \quad (11)$$

Assuming that the constant  $C_0$  is known, or that it can be determined from previous studies (Soulsby 1983; Souza 2013), Eq. (11) is only a function of the horizontal density gradient, the Coriolis parameter and the tidal frequency. We show below that this expression provides a simple prediction for the occurrence of MITS and TMZ.

Figure 12 shows where our model simulations fall in the  $(SiStk_-^2, \Delta\varepsilon)$  parameter space. As discussed in sections 1 and 2, MITS in ROFI systems with progressive tides, such as the Rhine, is generated by the counterrotating surface and bottom currents that result in the

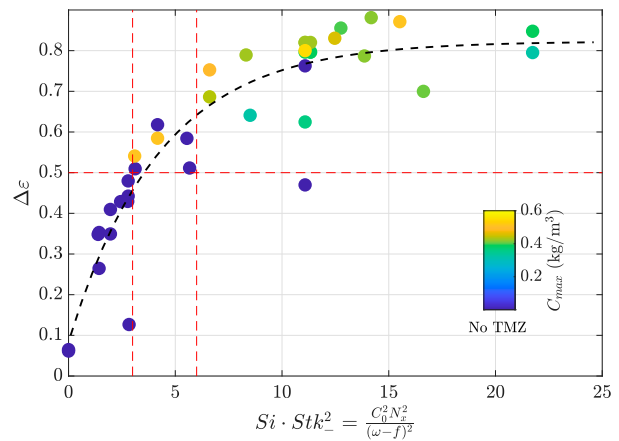


FIG. 12. Parameter space for MITS and turbidity maximum zones in coastal seas. The color bar indicates peak sediment concentrations observed in the TMZ. Zero concentration (dark blue) was assigned to runs where a TMZ was not observed. Dashed red lines indicate  $\Delta\varepsilon$  and  $SiStk_-^2$  threshold values for TMZ occurrence. The region between  $SiStk_-^2 = 3$  and  $SiStk_-^2 = 6$  is considered a transitional band in which a TMZ may occur, provided top–bottom ellipticity difference is greater than 0.5.

semidiurnal straining of the density field. Visser et al. (1994) suggest that high values of  $\Delta\varepsilon$  are associated with a significant degree of decoupling between the upper and lower layers, thus we use  $\Delta\varepsilon$  as an indicator of tidal straining. The relationship between  $SiStk_-^2$  and  $\Delta\varepsilon$  is clear; low values of  $\Delta\varepsilon$  occur at low  $SiStk_-^2$ , while high  $\Delta\varepsilon$  values occur at high  $SiStk_-^2$  (Fig. 12). This reflects the fact that the combination of horizontal buoyancy forcing and rotational frequency in  $SiStk_-^2$  accurately represents the balance required for the occurrence of tidal straining. High values of  $SiStk_-^2$  occur at moderate to high horizontal density gradients and at locations where  $\omega \approx f$  (midlatitudes), which is exactly where tidal straining is observed (e.g., Simpson and Souza 1995; Palmer 2010; Rijnsburger et al. 2016). On the other hand, low values of  $SiStk_-^2$  would typically occur at low latitudes  $\omega \neq f$  with low horizontal buoyancy forcing, where tidal straining is not expected to occur.

With the exception of one run, model runs for which  $\Delta\varepsilon \geq 0.5$  all have values of  $SiStk_-^2$  exceeding 6 (Fig. 12), suggesting that a limiting condition for the occurrence of MITS in progressive tide ROFI systems can be taken as  $SiStk_-^2 = 6$ . The occurrence of a TMZ is linked to the occurrence of MITS, as indicated by the color bar in Fig. 12. This is also in line with the results shown in Fig. 9, where the TMZ was only observed in regions of high  $\Delta\varepsilon$ . The peak suspended sediment concentrations in the TMZs are variable and typically range from 0.3 to  $0.6 \text{ kg m}^{-3}$  and, while there is no apparent correlation between the observed peak concentrations and  $SiStk_-^2$  or  $\Delta\varepsilon$ , it is clear that a TMZ generally occurs for runs

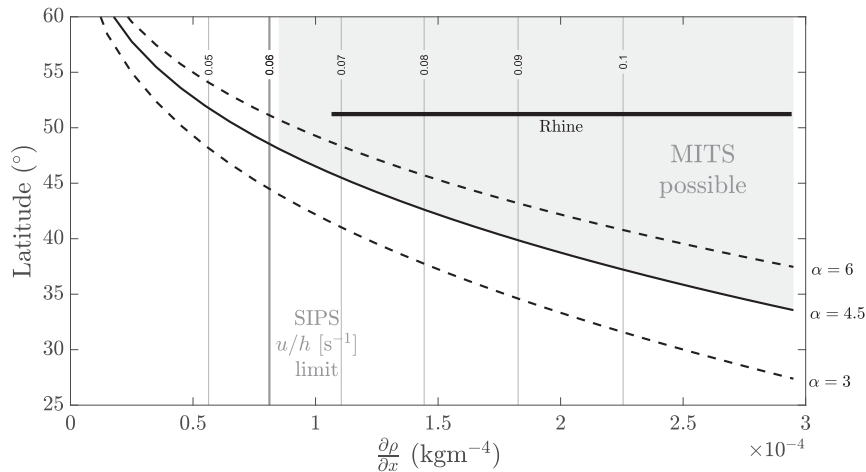


FIG. 13. Relationship between the horizontal density gradient and latitude, given by Eq. (12). Contours indicate the limiting  $u/h$  ( $\text{s}^{-1}$ ) value provided by the Simpson et al. (1990) SIPS condition for a given horizontal density gradient. The gray area defines where MITS is possible given a  $u/h$  ratio of 0.06, which is typical of the Rhine area. The horizontal black line indicates where our model results lay according to the horizontal density gradients observed in the simulations (e.g., Fig. 4).

with  $\text{SiStk}_x^2 \geq 6$  and  $\Delta\epsilon > 0.5$ . Model runs with no TMZ were assigned zero suspended sediment concentration (blue), even though concentrations can also be high (e.g., Fig. 9b).

Combining what is observed in Fig. 12 for the occurrence of MITS and the TMZ, the region  $3 \leq \text{SiStk}_x^2 \leq 6$  can be interpreted as a transitional band; for  $\text{SiStk}_x^2 < 3$  neither MITS or a TMZ occur whereas for  $\text{SiStk}_x^2 > 6$  they generally occur in our simulations. Taking  $\text{SiStk}_x^2 = \alpha$ , with  $\alpha$  in the range of 3–6, we can rewrite Eq. (11) as

$$N_x^2 \geq \alpha \frac{(\omega - f)^2}{C_0^2}, \quad (12)$$

where  $N_x^2 = -(g/\rho_0)\partial\rho/\partial x$ . Equation (12), which is plotted in Fig. 13, predicts the minimum value of the horizontal density gradient that would be required at a specific latitude for the occurrence of MITS. For example, for a typical cross-shore density gradient of  $1.5 \times 10^{-4} \text{ kg m}^{-4}$ , the minimum latitude at which MITS is expected to occur is approximately  $37^\circ$ . Alternatively, at a latitude of  $25^\circ$ , Eq. (12) indicates that a cross-shore density gradient of approximately  $5 \times 10^{-4} \text{ kg m}^{-4}$  is required for MITS to occur. This value is far larger than conditions typically observed in buoyant coastal currents and suggests that MITS will not occur at low latitudes given realistic values for the horizontal density gradient. As shown in section 5b, and additional constraint for the occurrence of MITS is water depth, which is given by the SIPS limiting condition [Eq. (10)]. The SIPS limiting condition is included in Fig. 13 in terms of

$u/h$  contours. For the case of the Rhine, where  $u/h \approx 0.06$ , the region of MITS occurrence is located to the right of the  $u/h = 0.06$  contour and above the line given by Eq. (12). Similarly, a region of MITS occurrence can be obtained for locations with other  $u/h$  values.

Overall, we find that the parameter space given by  $\text{SiStk}_x^2$  and  $\Delta\epsilon$  provides a simple approach to evaluate whether MITS could occur in shallow coastal regions for a given combination of density gradient, tidal velocity, depth and latitude. Provided there is a source of fine sediment to the system, this parameter space also predicts where a coastal TMZ similar to the one shown in Fig. 2 may form.

## 6. Conclusions

This work was motivated by field observations of a persistent offshore turbidity maximum zone (TMZ) that extends for tens of kilometers along the coast in the Rhine ROFI system (van Alphen 1990; Joordens et al. 2001; van der Hout et al. 2015). The aim of this study was to answer the following questions: can minor axis tidal straining (MITS) lead to the formation of an offshore TMZ? And what are the mechanisms that lead to cross-shore sediment convergence?

The major result of this idealized numerical modeling study is that MITS can lead to the formation of offshore turbidity maximum zones in ROFI systems with progressive tides. Our model simulations qualitatively reproduced the main dynamical features that are observed in the far field of the Rhine ROFI, which include

the semidiurnal variations in stratification and the modification of the tidal ellipses (Visser et al. 1994; Simpson and Souza 1995; de Boer et al. 2006; Souza et al. 2008). Model simulated location and size of the TMZ are similar to that observed in the field (van der Hout et al. 2015, 2017).

The cross-shore convergence in the subtidal near-bed sediment fluxes is driven by asymmetries in eddy viscosity that result from MITS dynamics. On a subtidal time scale, the asymmetries in eddy viscosity lead to landward cross-shore velocities in the near-bed region and landward subtidal sediment fluxes in water depths greater than approximately 12–15 m. The mechanism leading to landward residual sediment fluxes was found to be similar to the tidal straining mechanism that is observed to contribute to the formation of turbidity maximum zones in estuaries (Jay and Musiak 1994; Geyer et al. 2001). The cross-shore structure of the asymmetries in vertical mixing was found to explain the magnitude and direction of subtidal sediment fluxes, and, by extension, the position of the TMZ and the magnitude of the observed suspended sediment concentrations.

The location and extension of the TMZ, and magnitude of the suspended sediment concentrations strongly depend on the settling velocity and thus the Rouse number. As the settling velocity depends primarily on particle size, the dynamics of the TMZ and its generation are expected to vary according to the particle size distribution of fine bed sediments. The formation of a TMZ was observed for settling velocities as high as  $0.8\text{--}1\text{ mm s}^{-1}$  (silts), although its magnitude and relative importance with respect to concentrations in shallow water decreased with increasing settling velocity.

The Simpson and the Stokes numbers, in combination with the top–bottom tidal current ellipticity difference, were shown to provide a parameter space that successfully mapped the occurrence of MITS and a coastal TMZ in our simulations. In general, we observed that MITS only occurred at values of  $\text{SiStk}_2^2 > 3$ . The information needed to estimate  $\text{SiStk}_2^2$  is frequently available from field observations, such that the parameter space provided by Figs. 12 and 13 can be readily used to evaluate whether MITS can occur in a specific coastal region. Evaluation of limiting cases in terms of the required horizontal density gradients and latitudes suggests that MITS will not occur at low latitudes (less than  $25^\circ$ ). It should be noted that this study is limited to coastal seas with shallow bathymetries in which the variations in the cross-shore density gradients are the dominant dynamical feature. Nonetheless, these results can be relevant for several regions with progressive tides in midlatitudes and may encourage future research

regarding the occurrence of coastal TMZs in regions of freshwater influence.

Finally, the MITS mechanism reproduced here is just one of the potential mechanisms that can contribute to the formation of a coastal TMZ. Cross-shore transport near the bed may also result from a wide variety of physical processes, such as wave-driven bottom streaming, wind-induced downwelling or upwelling (Lentz and Fewings 2012), Stokes drift (Lentz and Fewings 2012), or gravity-driven sediment flows during extreme weather conditions (Traykovski et al. 2007; Flores et al. 2018). It is likely that all these mechanisms (and others) contribute to the maintenance of the TMZ over long time scales.

*Acknowledgments.* The authors thank Carola M. van der Hout for kindly providing the field data shown in Fig. 2a. The authors are also grateful for early conversations with G. J. de Boer about tidal straining in the Rhine ROFI and its impact on sediment transport. Model simulations were conducted in a high-performance computing machine maintained by Serhad Atakturk and Nick Burmeister. R.P. Flores is grateful for support from Fulbright and CONICYT-Chile (Becas Chile Program). A. Horner-Devine was supported by the Allan and Inger Osberg Professorship. N. Kumar acknowledges support from the Office of Naval Research, Littoral and Geosciences Division (N00014-17-1-2890). The authors are grateful for support from the Netherlands Organization for Scientific Research (STW), Sustainable ROFI's program Project 12682.

## REFERENCES

- Baumert, H., and G. Radach, 1992: Hysteresis of turbulent kinetic energy in nonrotational tidal flows: A model study. *J. Geophys. Res. Oceans*, **97**, 3669–3677, <https://doi.org/10.1029/91JC02717>.
- Brown, J. M., L. O. Amoudry, A. J. Souza, and J. Rees, 2015: Fate and pathways of dredged estuarine sediment spoil in response to variable sediment size and baroclinic coastal circulation. *J. Environ. Manage.*, **149**, 209–221, <https://doi.org/10.1016/j.jenvman.2014.10.017>.
- Burchard, H., and R. D. Hetland, 2010: Quantifying the contributions of tidal straining and gravitational circulation to residual circulation in periodically stratified tidal estuaries. *J. Phys. Oceanogr.*, **40**, 1243–1262, <https://doi.org/10.1175/2010JPO4270.1>.
- , and H. M. Schuttelaars, 2012: Analysis of tidal straining as driver for estuarine circulation in well-mixed estuaries. *J. Phys. Oceanogr.*, **42**, 261–271, <https://doi.org/10.1175/JPO-D-11-0110.1>.
- , G. Flöser, J. V. Staneva, T. H. Badewien, and R. Riethmüller, 2008: Impact of density gradients on net sediment transport into the Wadden Sea. *J. Phys. Oceanogr.*, **38**, 566–587, <https://doi.org/10.1175/2007JPO3796.1>.
- , H. M. Schuttelaars, and W. R. Geyer, 2013: Residual sediment fluxes in weakly-to-periodically stratified estuaries and

- tidal inlets. *J. Phys. Oceanogr.*, **43**, 1841–1861, <https://doi.org/10.1175/JPO-D-12-0231.1>.
- , —, and D. K. Ralston, 2018: Sediment trapping in estuaries. *Annu. Rev. Mar. Sci.*, **10**, 371–395, <https://doi.org/10.1146/annurev-marine-010816-060535>.
- Chapman, D. C., and S. J. Lentz, 1997: Adjustment of stratified flow over a sloping bottom. *J. Phys. Oceanogr.*, **27**, 340–356, [https://doi.org/10.1175/1520-0485\(1997\)027<0340:AOSFOA>2.0.CO;2](https://doi.org/10.1175/1520-0485(1997)027<0340:AOSFOA>2.0.CO;2).
- Chen, S.-N., W. R. Geyer, and T.-J. Hsu, 2013: A numerical investigation of the dynamics and structure of hyperviscous river plumes on sloping continental shelves. *J. Geophys. Res. Oceans*, **118**, 2702–2718, <https://doi.org/10.1002/jgrc.20209>.
- de Boer, G. J., J. D. Pietrzak, and J. C. Winterwerp, 2006: On the vertical structure of the Rhine region of freshwater influence. *Ocean Dyn.*, **56**, 198–216, <https://doi.org/10.1007/s10236-005-0042-1>.
- , —, and —, 2008: Using the potential energy anomaly equation to investigate tidal straining and advection of stratification in a region of freshwater influence. *Ocean Modell.*, **22**, 1–11, <https://doi.org/10.1016/j.ocemod.2007.12.003>.
- Eisma, D., 1990: Transport and deposition of suspended matter in the North-Sea and the relation to coastal siltation, pollution, and bottom fauna distribution. *Rev. Aquat. Sci.*, **3**, 181–216.
- Fischer, E., H. Burchard, and R. D. Hetland, 2009: Numerical investigations of the turbulent kinetic energy dissipation rate in the Rhine region of freshwater influence. *Ocean Dyn.*, **59**, 629–641, <https://doi.org/10.1007/s10236-009-0187-4>.
- Fisher, N., J. Simpson, and M. Howarth, 2002: Turbulent dissipation in the Rhine ROFI forced by tidal flow and wind stress. *J. Sea Res.*, **48**, 249–258, [https://doi.org/10.1016/S1385-1101\(02\)00194-6](https://doi.org/10.1016/S1385-1101(02)00194-6).
- Flores, R. P., S. Rijnsburger, A. R. Horner-Devine, A. J. Souza, and J. D. Pietrzak, 2017: The impact of storms and stratification on sediment transport in the Rhine region of freshwater influence. *J. Geophys. Res. Oceans*, **122**, 4456–4477, <https://doi.org/10.1002/2016JC012362>.
- , —, S. Meirelles, A. R. Horner-Devine, A. J. Souza, J. D. Pietrzak, M. Henriquez, and A. Reniers, 2018: Wave generation of gravity-driven sediment flows on a predominantly sandy seabed. *Geophys. Res. Lett.*, **45**, 7634–7645, <https://doi.org/10.1029/2018GL077936>.
- Geyer, W. R., 1993: The importance of suppression of turbulence by stratification on the estuarine turbidity maximum. *Estuaries*, **16**, 113–125, <https://doi.org/10.2307/1352769>.
- , and P. MacCready, 2014: The estuarine circulation. *Annu. Rev. Fluid Mech.*, **46**, 175–197, <https://doi.org/10.1146/annurev-fluid-010313-141302>.
- , J. H. Trowbridge, and M. M. Bowen, 2000: The dynamics of a partially mixed estuary. *J. Phys. Oceanogr.*, **30**, 2035–2048, [https://doi.org/10.1175/1520-0485\(2000\)030<2035:TDOAPM>2.0.CO;2](https://doi.org/10.1175/1520-0485(2000)030<2035:TDOAPM>2.0.CO;2).
- , J. D. Woodruff, and P. Traykovski, 2001: Sediment transport and trapping in the Hudson River estuary. *Estuaries*, **24**, 670–679, <https://doi.org/10.2307/1352875>.
- , P. Hill, and G. Kineke, 2004: The transport, transformation and dispersal of sediment by buoyant coastal flows. *Cont. Shelf Res.*, **24**, 927–949, <https://doi.org/10.1016/j.csr.2004.02.006>.
- Godin, G., 1972: *The Analysis of Tides*. Liverpool University Press, 264 pp.
- Hansen, D. V., and M. Rattray, 1965: Gravitational circulation in straits and estuaries. *J. Mar. Res.*, **23**, 104–122.
- Harris, C. K., C. R. Sherwood, R. P. Signell, A. J. Bever, and J. C. Warner, 2008: Sediment dispersal in the northwestern Adriatic Sea. *J. Geophys. Res.*, **113**, C11S03, <https://doi.org/10.1029/2006JC003868>.
- Horner-Devine, A. R., R. D. Hetland, and D. G. MacDonald, 2015: Mixing and transport in coastal river plumes. *Annu. Rev. Fluid Mech.*, **47**, 569–594, <https://doi.org/10.1146/annurev-fluid-010313-141408>.
- , J. D. Pietrzak, A. J. Souza, M. A. McKeon, S. Meirelles, M. Henriquez, R. P. Flores, and S. Rijnsburger, 2017: Cross-shore transport of nearshore sediment by river plume frontal pumping. *Geophys. Res. Lett.*, **44**, 6343–6351, <https://doi.org/10.1002/2017GL073378>.
- Horwitz, R., and S. J. Lentz, 2014: Inner-shelf response to cross-shelf wind stress: The importance of the cross-shelf density gradient in an idealized numerical model and field observations. *J. Phys. Oceanogr.*, **44**, 86–103, <https://doi.org/10.1175/JPO-D-13-075.1>.
- Huisman, B., M. De Schipper, and B. Ruessink, 2016: Sediment sorting at the Sand Motor at storm and annual time scales. *Mar. Geol.*, **381**, 209–226, <https://doi.org/10.1016/j.margeo.2016.09.005>.
- Hunt, J., 1954: The turbulent transport of suspended sediment in open channels. *Proc. Roy. Soc. London*, **224A**, 322–335, <https://doi.org/10.1098/rspa.1954.0161>.
- Huthnance, J., 1991: Physical oceanography of the North Sea. *Ocean Shoreline Manage.*, **16**, 199–231, [https://doi.org/10.1016/0951-8312\(91\)90005-M](https://doi.org/10.1016/0951-8312(91)90005-M).
- Jacobs, W., 2004: Modelling the Rhine river plume. M.Sc. thesis, Faculty of Civil Engineering and Geosciences, Hydraulic Engineering, Delft University of Technology, 135 pp.
- Jay, D. A., and J. D. Musiak, 1994: Particle trapping in estuarine tidal flows. *J. Geophys. Res.*, **99**, 20 445–20 461, <https://doi.org/10.1029/94JC00971>.
- Joordens, J., A. Souza, and A. Visser, 2001: The influence of tidal straining and wind on suspended matter and phytoplankton distribution in the Rhine outflow region. *Cont. Shelf Res.*, **21**, 301–325, [https://doi.org/10.1016/S0278-4343\(00\)00095-9](https://doi.org/10.1016/S0278-4343(00)00095-9).
- Kumar, N., F. Feddersen, Y. Uchiyama, J. McWilliams, and W. O'Reilly, 2015: Midshelf to surfzone coupled ROMS–SWAN model data comparison of waves, currents, and temperature: Diagnosis of subtidal forcings and response. *J. Phys. Oceanogr.*, **45**, 1464–1490, <https://doi.org/10.1175/JPO-D-14-0151.1>.
- Lentz, S. J., and M. R. Fewings, 2012: The wind-and wave-driven inner-shelf circulation. *Annu. Rev. Mar. Sci.*, **4**, 317–343, <https://doi.org/10.1146/annurev-marine-120709-142745>.
- Lerczak, J. A., and R. Geyer, 2004: Modeling the lateral circulation in straight, stratified estuaries. *J. Phys. Oceanogr.*, **34**, 1410–1428, [https://doi.org/10.1175/1520-0485\(2004\)034<1410:MTLCIS>2.0.CO;2](https://doi.org/10.1175/1520-0485(2004)034<1410:MTLCIS>2.0.CO;2).
- Marchesiello, P., J. C. McWilliams, and A. Shchepetkin, 2001: Open boundary conditions for long-term integration of regional oceanic models. *Ocean Modell.*, **3**, 1–20, [https://doi.org/10.1016/S1463-5003\(00\)00013-5](https://doi.org/10.1016/S1463-5003(00)00013-5).
- Monismith, S., J. Burau, and M. Stacey, 1996: Stratification dynamics and gravitational circulation in Northern San Francisco Bay. *San Francisco Bay: The Ecosystem*, J. T. Hollibaugh, Ed., American Association for the Advancement of Science, 123–153.
- Nidzicko, N. J., J. L. Hench, and S. G. Monismith, 2009: Lateral circulation in well-mixed and stratified estuarine flows with curvature. *J. Phys. Oceanogr.*, **39**, 831–851, <https://doi.org/10.1175/2008JPO4017.1>.
- Palmer, M. R., 2010: The modification of current ellipses by stratification in the Liverpool Bay ROFI. *Ocean Dyn.*, **60**, 219–226, <https://doi.org/10.1007/s10236-009-0246-x>.

- Pietrzak, J. D., G. J. de Boer, and M. A. Eleveld, 2011: Mechanisms controlling the intra-annual mesoscale variability of SST and SPM in the southern North Sea. *Cont. Shelf Res.*, **31**, 594–610, <https://doi.org/10.1016/j.csr.2010.12.014>.
- Prandle, D., 1982: The vertical structure of tidal currents and other oscillatory flows. *Cont. Shelf Res.*, **1**, 191–207, [https://doi.org/10.1016/0278-4343\(82\)90004-8](https://doi.org/10.1016/0278-4343(82)90004-8).
- Rijnsburger, S., C. M. van der Hout, O. van Tongeren, G. J. de Boer, B. C. van Prooijen, W. G. Borst, and J. D. Pietrzak, 2016: Simultaneous measurements of tidal straining and advection at two parallel transects far downstream in the Rhine ROFI. *Ocean Dyn.*, **66**, 719–736, <https://doi.org/10.1007/s10236-016-0947-x>.
- , R. P. Flores, J. D. Pietrzak, A. R. Horner-Devine, and A. J. Souza, 2018: The influence of tide and wind on the propagation of fronts in a shallow river plume. *J. Geophys. Res. Oceans*, **123**, 5426–5442, <https://doi.org/10.1029/2017JC013422>.
- Rippeth, T. P., N. R. Fisher, and J. H. Simpson, 2001: The cycle of turbulent dissipation in the presence of tidal straining. *J. Phys. Oceanogr.*, **31**, 2458–2471, [https://doi.org/10.1175/1520-0485\(2001\)031<2458:TCOTDI>2.0.CO;2](https://doi.org/10.1175/1520-0485(2001)031<2458:TCOTDI>2.0.CO;2).
- Roos, P. C., J. J. Velema, S. J. Hulscher, and A. Stolk, 2011: An idealized model of tidal dynamics in the North Sea: Resonance properties and response to large-scale changes. *Ocean Dyn.*, **61**, 2019–2035, <https://doi.org/10.1007/s10236-011-0456-x>.
- Rouse, H., 1937: Modern conceptions of the mechanics of fluid turbulence. *Trans. Amer. Soc. Civ. Eng.*, **102**, 463–505.
- Ruddick, K., E. Deleersnijder, P. Luyten, and J. Ozer, 1995: Haline stratification in the Rhine-Meuse freshwater plume: A three-dimensional model sensitivity analysis. *Cont. Shelf Res.*, **15**, 1597–1630, [https://doi.org/10.1016/0278-4343\(95\)00034-X](https://doi.org/10.1016/0278-4343(95)00034-X).
- Sanford, L. P., and J. P.-Y. Maa, 2001: A unified erosion formulation for fine sediments. *Mar. Geol.*, **179**, 9–23, [https://doi.org/10.1016/S0025-3227\(01\)00201-8](https://doi.org/10.1016/S0025-3227(01)00201-8).
- Schulz, K., and L. Umlauf, 2016: Residual transport of suspended material by tidal straining near sloping topography. *J. Phys. Oceanogr.*, **46**, 2083–2102, <https://doi.org/10.1175/JPO-D-15-0218.1>.
- Scully, M. E., and C. T. Friedrichs, 2007: Sediment pumping by tidal asymmetry in a partially mixed estuary. *J. Geophys. Res.*, **112**, C07028, <https://doi.org/10.1029/2006JC003784>.
- Shchepetkin, A. F., and J. C. McWilliams, 2005: The regional oceanic modeling system (ROMS): A split-explicit, free-surface, topography-following-coordinate oceanic model. *Ocean Modell.*, **9**, 347–404, <https://doi.org/10.1016/j.ocemod.2004.08.002>.
- Simpson, J. H., 1997: Physical processes in the ROFI regime. *J. Mar. Syst.*, **12**, 3–15, [https://doi.org/10.1016/S0924-7963\(96\)00085-1](https://doi.org/10.1016/S0924-7963(96)00085-1).
- , and A. Souza, 1995: Semidiurnal switching of stratification in the region of freshwater influence of the Rhine. *J. Geophys. Res.*, **100**, 7037–7044, <https://doi.org/10.1029/95JC00067>.
- , J. Brown, J. Matthews, and G. Allen, 1990: Tidal straining, density currents, and stirring in the control of estuarine stratification. *Estuaries*, **13**, 125–132, <https://doi.org/10.2307/1351581>.
- , W. G. Bos, F. Schirmer, A. J. Souza, T. P. Rippeth, S. E. Jones, and D. Hydes, 1993: Periodic stratification in the Rhine ROFI in the North Sea. *Oceanol. Acta*, **16**, 23–32.
- Soulsby, R. L., 1983: The bottom boundary layer of shelf seas. *Physical Oceanography of Coastal and Shelf Seas*, Elsevier Oceanography Series, Vol. 35, Elsevier, 189–266, [https://doi.org/10.1016/S0422-9894\(08\)70503-8](https://doi.org/10.1016/S0422-9894(08)70503-8).
- Souza, A. J., 2013: On the use of the Stokes number to explain frictional tidal dynamics and water column structure in shelf seas. *Ocean Sci.*, **9**, 391–398, <https://doi.org/10.5194/os-9-391-2013>.
- , and I. James, 1996: A two-dimensional (xz) model of tidal straining in the Rhine ROFI. *Cont. Shelf Res.*, **16**, 949–966, [https://doi.org/10.1016/0278-4343\(95\)00033-X](https://doi.org/10.1016/0278-4343(95)00033-X).
- , and J. H. Simpson, 1996: The modification of tidal ellipses by stratification in the Rhine ROFI. *Cont. Shelf Res.*, **16**, 997–1007, [https://doi.org/10.1016/0278-4343\(95\)00042-9](https://doi.org/10.1016/0278-4343(95)00042-9).
- , and A. Lane, 2013: Effects of freshwater inflow on sediment transport. *J. Oper. Oceanogr.*, **6**, 27–31, <https://doi.org/10.1080/1755876X.2013.11020143>.
- , J. H. Simpson, and F. Schirmer, 1997: Current structure in the Rhine region of freshwater influence. *J. Mar. Res.*, **55**, 277–292, <https://doi.org/10.1357/0022240973224409>.
- , N. R. Fisher, J. H. Simpson, and M. J. Howarth, 2008: Effects of tidal straining on the semidiurnal cycle of dissipation in the Rhine region of freshwater influence: Comparison of model and measurements. *J. Geophys. Res.*, **113**, C01011, <https://doi.org/10.1029/2006JC004002>.
- Stacey, M. T., S. G. Monismith, and J. R. Burau, 1999: Observations of turbulence in a partially stratified estuary. *J. Phys. Oceanogr.*, **29**, 1950–1970, [https://doi.org/10.1175/1520-0485\(1999\)029<1950:OOTIAP>2.0.CO;2](https://doi.org/10.1175/1520-0485(1999)029<1950:OOTIAP>2.0.CO;2).
- , J. R. Burau, and S. G. Monismith, 2001: Creation of residual flows in a partially stratified estuary. *J. Geophys. Res.*, **106**, 17 013–17 037, <https://doi.org/10.1029/2000JC000576>.
- , M. L. Brennan, J. R. Burau, and S. G. Monismith, 2010: The tidally averaged momentum balance in a partially and periodically stratified estuary. *J. Phys. Oceanogr.*, **40**, 2418–2434, <https://doi.org/10.1175/2010JPO4389.1>.
- Stive, M. J., and Coauthors, 2013: A new alternative to saving our beaches from sea-level rise: The Sand Engine. *J. Coastal Res.*, **29**, 1001–1008, <https://doi.org/10.2112/JCOASTRES-D-13-00070.1>.
- Stokes, G. G., 1851: On the effect of the internal friction of fluids on the motion of pendulums. *Trans. Cambridge Philos. Soc.*, **9**, Part II, 99 pp.
- Traykovski, P., P. L. Wiberg, and W. R. Geyer, 2007: Observations and modeling of wave-supported sediment gravity flows on the Po prodelta and comparison to prior observations from the Eel shelf. *Cont. Shelf Res.*, **27**, 375–399, <https://doi.org/10.1016/j.csr.2005.07.008>.
- Umlauf, L., and H. Burchard, 2003: A generic length-scale equation for geophysical turbulence models. *J. Mar. Res.*, **61**, 235–265, <https://doi.org/10.1357/002224003322005087>.
- van Alphen, J. S. L. J., 1990: A mud balance for Belgian-Dutch coastal waters between 1969 and 1986. *Neth. J. Sea Res.*, **25**, 19–30, [https://doi.org/10.1016/0077-7579\(90\)90005-2](https://doi.org/10.1016/0077-7579(90)90005-2).
- van der Hout, C. M., T. Gerkema, J. J. Nauw, and H. Ridderinkhof, 2015: Observations of a narrow zone of high suspended particulate matter (SPM) concentrations along the Dutch coast. *Cont. Shelf Res.*, **95**, 27–38, <https://doi.org/10.1016/j.csr.2015.01.002>.
- , R. Witbaard, M. Bergman, G. Duineveld, M. Rozemeijer, and T. Gerkema, 2017: The dynamics of suspended particulate matter (SPM) and chlorophyll-a from intratidal to annual time scales in a coastal turbidity maximum. *J. Sea Res.*, **127**, 105–118, <https://doi.org/10.1016/j.seares.2017.04.011>.
- Verspecht, F., J. Simpson, and T. Rippeth, 2010: Semi-diurnal tidal ellipse variability in a region of freshwater influence. *Geophys. Res. Lett.*, **37**, L18602, <https://doi.org/10.1029/2010GL044470>.

- Visser, A., A. Souza, K. Hessner, and J. Simpson, 1994: The effect of stratification on tidal current profiles in a region of fresh-water influence. *Oceanol. Acta*, **17**, 369–381.
- Warner, J. C., C. R. Sherwood, H. G. Arango, and R. P. Signell, 2005: Performance of four turbulence closure models implemented using a generic length scale method. *Ocean Modell.*, **8**, 81–113, <https://doi.org/10.1016/j.ocemod.2003.12.003>.
- , B. Butman, and P. S. Dalyander, 2008a: Storm-driven sediment transport in Massachusetts Bay. *Cont. Shelf Res.*, **28**, 257–282, <https://doi.org/10.1016/j.csr.2007.08.008>.
- , C. R. Sherwood, R. P. Signell, C. K. Harris, and H. G. Arango, 2008b: Development of a three-dimensional, regional, coupled wave, current, and sediment-transport model. *Comput. Geosci.*, **34**, 1284–1306, <https://doi.org/10.1016/j.cageo.2008.02.012>.
- Winant, C. D., 2007: Three-dimensional tidal flow in an elongated, rotating basin. *J. Phys. Oceanogr.*, **37**, 2345–2362, <https://doi.org/10.1175/JPO3122.1>.
- Wu, H., J. Shen, J. Zhu, J. Zhang, and L. Li, 2014: Characteristics of the Changjiang plume and its extension along the Jiangsu coast. *Cont. Shelf Res.*, **76**, 108–123, <https://doi.org/10.1016/j.csr.2014.01.007>.
- Yoshiyama, K., and J. H. Sharp, 2006: Phytoplankton response to nutrient enrichment in an urbanized estuary: Apparent inhibition of primary production by overeutrophication. *Limnol. Oceanogr.*, **51**, 424–434, [https://doi.org/10.4319/lo.2006.51.1\\_part\\_2.0424](https://doi.org/10.4319/lo.2006.51.1_part_2.0424).